

# JGR Solid Earth

## RESEARCH ARTICLE

10.1029/2021JB022779

### Key Points:

- Improved the correction method for long wavelength orbital ramps to obtain a more accurate Planet-Lab horizontal displacement field
- Resolved and separated the detailed slip distributions of the foreshock and mainshock using the GPS and dense Planet-Lab optical data
- Improved source modeling through the combined use of InSAR, SAR, GPS, and optical datasets

### Supporting Information:

Supporting Information may be found in the online version of this article.

### Correspondence to:

G. Feng,  
fredgps@csu.edu.cn

### Citation:

He, L., Feng, G., Hu, J., Xu, W., Liu, J., Li, Z., et al. (2022). Surface displacement and source model separation of the two strongest earthquakes during the 2019 Ridgecrest sequence: Insights from InSAR, GPS, and optical data. *Journal of Geophysical Research: Solid Earth*, 127, e2021JB022779. <https://doi.org/10.1029/2021JB022779>

Received 16 JUL 2021  
Accepted 25 JAN 2022

### Author Contributions:

**Conceptualization:** Lijia He  
**Data curation:** Lijia He, Jihong Liu  
**Formal analysis:** Lijia He, Guangcai Feng, Jun Hu, Wenbin Xu, Jihong Liu, Zhiwei Li, Zhixiong Feng, Yuedong Wang, Hao Lu  
**Methodology:** Lijia He  
**Resources:** Lijia He, Guangcai Feng, Jun Hu, Zhiwei Li  
**Software:** Lijia He, Guangcai Feng  
**Validation:** Lijia He, Guangcai Feng, Zhixiong Feng, Yuedong Wang, Hao Lu  
**Visualization:** Lijia He  
**Writing – original draft:** Lijia He  
**Writing – review & editing:** Lijia He, Guangcai Feng

© 2022. American Geophysical Union.  
All Rights Reserved.

## Surface Displacement and Source Model Separation of the Two Strongest Earthquakes During the 2019 Ridgecrest Sequence: Insights From InSAR, GPS, and Optical Data

Lijia He<sup>1,2</sup> , Guangcai Feng<sup>1,2</sup> , Jun Hu<sup>1,2</sup> , Wenbin Xu<sup>1,2</sup> , Jihong Liu<sup>1,2</sup> , Zhiwei Li<sup>1,2</sup> , Zhixiong Feng<sup>1,2</sup> , Yuedong Wang<sup>1,2</sup> , and Hao Lu<sup>1,2</sup> 

<sup>1</sup>Laboratory of Radar Remote Sensing, School of Geosciences and Info-Physics, Central South University, Changsha, China,

<sup>2</sup>Key Laboratory of Metallogenic Prediction of Nonferrous Metals and Geological Environment Monitoring, Central South University, Changsha, China

**Abstract** Since the occurrence of the 2019  $M_w$  6.4 and  $M_w$  7.1 Ridgecrest earthquake sequence in the Eastern California Shear Zone, coseismic deformation following the two earthquakes has been intensively studied, and source modeling with interferometric synthetic aperture radar (InSAR), Global Positioning System (GPS) and seismological datasets has been favored. However, we recently found that the coseismic modeling of the two earthquakes constrained by the dense near-field Planet-Lab optical measurements can be more detailed than the previously estimated, which requires an accurate Planet-Lab displacement. In this study, we improve the long wavelength orbital ramps correction method for obtaining a more accurate Planet-Lab horizontal displacement field. The corrected dense near-field Planet-Lab data are firstly used together with the intermediate-field GPS data to invert and distinguish the fault slip distribution for the two earthquakes. The same scheme is used to simultaneously invert the InSAR, SAR, GPS, and optical datasets, to improve the constraints on seismic source parameters. Our inversion results show that the joint-event slip model is rougher than the two single-event slip models, but it has a more concentrated slip pattern and larger slip amplitude in some zones. We show that adding a near-field constraint of the Planet-Lab data in the combined-data inversion can reduce the slip parameter uncertainty and enhance the model resolution. The Coulomb failure stress changes on the southeastern Blackwater, the southern Owens Valley, and the central Panamint Valley faults are enhanced by about 0.4–0.8 bar by the 2019 Ridgecrest earthquake sequence.

**Plain Language Summary** In July 2019, an earthquake sequence, including an  $M_w$  6.4 foreshock on 4 July at 17:33 UTC and an  $M_w$  7.1 mainshock that occurred 34 hr later, struck the Ridgecrest, southern California. Previous studies have used the Planet-Lab data to extract the surface displacement of the respective events but ignored the long wavelength ramps in each block of the Planet-Lab image displacement field. We improve the correction method for long wavelength orbital ramps to obtain a more accurate Planet-Lab horizontal displacement field. The source model of individual events during an earthquake sequence is routinely inverted from seismic waveforms and/or GPS data, which, however, have difficulty in obtaining the detailed slip distributions, due to their low spatial density. We use the corrected Planet-Lab horizontal displacement to improve the near-field data constraints in source modeling. This work is the first application of using the Planet-Lab data to separate the fault slip model of the two strongest earthquakes during the Ridgecrest earthquake sequence, highlighting the importance of the high spatiotemporal resolution Planet-Lab data in refining fault geometry and restoring detailed fault slip distribution.

## 1. Introduction

Earthquakes with large magnitudes ( $M > 6$ ) in a sequence usually occurred closely in time and space, such as the sequences of the 2007 Mentawai (Konca et al., 2008), the 2012 Emilia (Tizzani et al., 2013), the 2014 Ziarat (Pinel-Puysségur et al., 2014), and the 2014 Kangding earthquakes (Jiang et al., 2015). The GPS stations are sparsely distributed in space and the space-based geodetic data (e.g., InSAR and optical observations) have limited samples in time, so the dense displacement field of individual events in an earthquake sequence is still hard to obtain and distinguish. Besides, their source models are routinely inverted from seismic waveforms and/or GPS data, which, however, have difficulty in obtaining the detailed slip distributions, due to the low spatial density.

The high spatiotemporal resolution Planet-Lab optical imagery can resolve those problems. Feng et al. (2019) analyzed the error characteristics of the Planet-Lab image displacement field and suggested that the long-wavelength orbit ramp is the major error source. They divided the Planet-Lab image displacement field of the 2018 Palu earthquake into several blocks according to the displacement discontinuities in the satellite along-track direction. Furthermore, they used a polynomial curve fitting method to remove the long-wavelength orbit ramps in each block and further obtained a displacement field with good continuity. However, when estimating the signal of orbit ramps, Feng et al. (2019) took the entire displacement field into account without masking the deformed area near the rupture, which might bias the estimated orbit ramps and the detrended displacement. Therefore, the long wavelength ramps in each block of the Planet-Lab image displacement field are generally difficult to correct if no external auxiliary information is available, resulting in the inability to restore an accurate surface displacement field. Additionally, such optical images are rarely used for source modeling, because their accuracy for coseismic displacement measurement is about 0.1–0.25 pixels (0.3–0.75 m; e.g., Feng et al., 2019; Kääh et al., 2017). Therefore, it is necessary to improve the measurement accuracy of the Planet-Lab optical data and use them to separate the detailed fault-slip distribution for individual events in an earthquake sequence.

In July 2019, an earthquake sequence, consisting of an  $M_w$  6.4 foreshock on 4 July at 17:33 UTC and an  $M_w$  7.1 mainshock that occurred 34 hr later, struck the Ridgecrest in the Eastern California Shear Zone, southern California (Figure 1). Those two earthquakes occurred closely in time and space and had the strike-slip mechanisms predominated by NE-SW-trending left-lateral and NW-SE-trending right-lateral sources, respectively (Ross et al., 2019). Many efforts have been made to estimate the cumulative fault slip models of the two events using the InSAR measurements (e.g., Barnhart et al., 2019; Chen et al., 2020; Feng et al., 2020; Goldberg et al., 2020; Jin & Fialko, 2020; Magen et al., 2020; Pollitz et al., 2020; Ross et al., 2019; Wang et al., 2020; X. Xu et al., 2020). Higher temporal resolution GPS and/or seismic waveform data, have been used to distinguish the rupture characteristics of individual events (e.g., C. Liu, Lay, et al., 2019; S. Li et al., 2020). The Planet-Lab imagery is a special kind of space-based geodetic data with high spatiotemporal resolution. Although the Planet-Lab data have been used in the surface displacement separation (e.g., Chen et al., 2020; Milliner & Donnellan, 2020), they have so far not been used to isolate the source model of individual events, due to the impact of the residual block-to-block orbital ramps in the deformation maps. In this case, the abundant geodetic data can be used to understand the interaction mechanisms of the two orthogonal seismogenic faults, and to investigate the discrepancies between the separate- and joint-event fault slip estimates.

In this study, we first use the sub-pixel correlation of Planet-Lab imagery, GPS observations, as well as InSAR, multiple aperture InSAR (MAI), and pixel offset-tracking (POT) measurements from Sentinel-1 and ALOS-2 SAR data to obtain the complete coseismic displacement fields caused by the 2019 Ridgecrest earthquake sequence. Next, we build four models in total for source modeling, including two single-event models (a foreshock-only model and a mainshock-only model), one joint-event model, and one combined-data model. Then, we perform slip parameter uncertainty analysis to investigate the robustness of different models, resolution analysis to evaluate the resolving power of different inversions, and sensitivity analysis to visualize the location where each dataset actually constrains slip. Finally, we discuss the capability of Planet-Lab data in fault slip separation, the difference in mode slip parameter uncertainty and resolution between different model inversions, the regional potential seismic hazard risks on surrounding active faults, and the limitations of the elastic homogeneity hypothesis.

## 2. Data and Method

In this study, we used three kinds of datasets, which are the SAR images from the C-band Sentinel-1 satellite with the Terrain Observation by Progressive Scans (TOPS) mode and the L-band Advanced Land Observing Satellite 2 (ALOS-2) satellite with the Scanning SAR (ScanSAR) mode (Table 1), the optical images from Planet-Lab satellites, and GPS data. The spatial coverage of these images is shown in Figure 1, and the location of GPS stations is shown in Figures S1 and S2 in Supporting Information S1.

### 2.1. SAR Images Processing

For SAR images, the differential InSAR (DInSAR; Gabriel et al., 1989), MAI (Bechor & Zebker, 2006), and POT (Michel et al., 1999) methods were employed to obtain the ground displacements along the line-of-sight

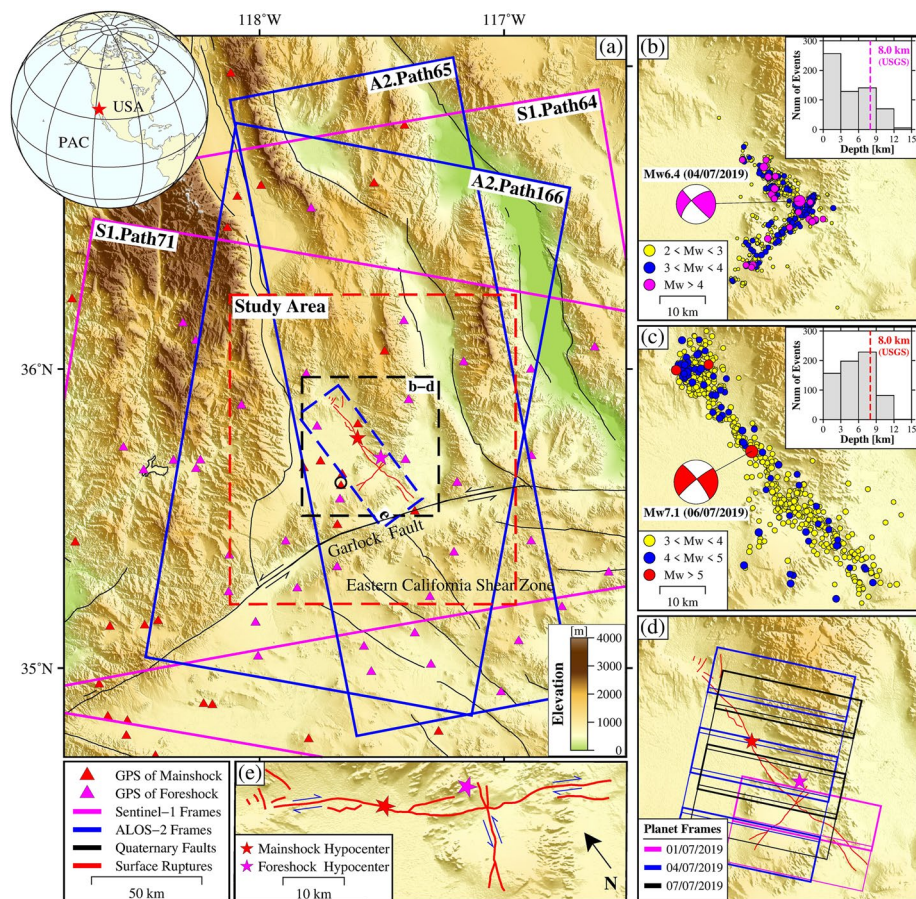


**Figure 1.** Overview of the regional seismogenic area of the 2019 Ridgecrest earthquake sequence on a color-shaded elevation map. (a) Spatial frames of Sentinel-1 (S1) (magenta heavy lines) and Advanced Land Observing Satellite 2 (A2) (blue heavy lines) synthetic aperture radar images were used in this study. The magenta and red stars are the locations of the foreshock ( $M_w$  6.4) and the mainshock ( $M_w$  7.1) hypocenters, respectively, given by the United States Geological Survey catalog. The magenta and red triangles indicate some global positioning system (GPS) sites for monitoring the foreshock and the mainshock, respectively. All GPS sites are shown in Figures S1 and S2 in Supporting Information S1. The red dashed box denotes the study area, as shown in Figures 2a–2h. The black and blue dashed boxes represent the regions shown in sub-graphs (b)–(d) and (e), respectively. The black circle marks the city of Ridgecrest. The red lines depict the footprints of the surface ruptures mapped by field investigation. The black lines outline some major quaternary crustal faults located in the vicinity of the Ridgecrest area, modified from Frankel et al. (2008). (b) Aftershock distribution ( $M > 2$ ) of the foreshock before the mainshock. (c) Aftershock distribution ( $M > 3$ ) in the first month following the mainshock. Events in (b) and (c) are color coded by moment magnitudes, and their depths are shown in the histograms. Beach balls display the focal mechanism solutions of these two events given by U.S. Geological Survey (2019a, 2019b) with labeled magnitudes and dates. (d) Spatial frames of the Planet-Lab optical imagery, color coded by the acquired dates. Dates in (b)–(d) are formatted as day/month/year. (e) Enlarged region of surface ruptures in (a) (red lines with blue labeled slip senses).

(LOS) and along-track directions with the GAMMA software (Werner et al., 2000), in which the shuttle radar topographic mission 1-arcsecond ( $\sim 30$  m spacing) digital elevation model (DEM) was utilized to remove the topographic contributions and correct possible coregistration misfits. We coregistered two single look complex images with the assistance of DEM. A multi-looking operation of  $30 \times 8$  and  $6 \times 32$  (range  $\times$  azimuth) was applied to Sentinel-1 and ALOS-2 interferograms, respectively. After minimizing the decorrelation noise with an improved Goldstein filter (Z. W. Li et al., 2008), the minimum cost flow method (Chen & Zebker, 2002) was used to unwrap the interferometric phase by masking the areas with coherence value smaller than 0.4.

The POT and MAI methods have lower accuracy than the DInSAR method, but they can extract the deformation along the along-track direction, which is crucial for interpreting geophysical phenomena with large surface displacements, such as earthquakes, glaciers, or volcanic movements. To measure the ground deformation by the POT method, the matching window size of  $300 \times 60$  pixels and  $40 \times 185$  pixels (range  $\times$  azimuth) was utilized

**Table 1**  
*InSAR and Optical Data Summary*

Sensor	Master image	Slave image	Days after foreshock	Days after mainshock	Pass	Path	Operation mode	Data processing method
ALOS-2	8 Aug. 2016	8 Jul. 2019	4	2	Asc.	65	ScanSAR	DInSAR + MAI
ALOS-2	2 Apr. 2019	23 Jul. 2019	19	17	Des.	166	ScanSAR	
Sentinel-1	4 Jul. 2019	10 Jul. 2019	6	4	Asc.	64	TOPS	DInSAR + POT
Sentinel-1	4 Jul. 2019	16 Jul. 2019	12	10	Des.	71	TOPS	
Planet-Lab	1 Jul. 2019	4 Jul. 2019	< 1	—	—	—	—	SPC
Planet-Lab	4 Jul. 2019	7 Jul. 2019	3	1	—	—	—	

for Sentinel-1 and ALOS-2 data, respectively (W. Xu et al., 2018). The MAI procedure was applied to both the ALOS-2 and Sentinel-1 data, but only the azimuth result of the former was selected because that of the latter has low coherence. The sub-aperture interferograms were generated on the framework of the DInSAR process (Liang & Fielding, 2017). These two sub-aperture interferograms were then differenced to generate the phase maps related to the azimuth deformation, which would be further filtered to derive the final along-track deformation. A directional filter was applied to the ascending ALOS-2 MAI interferogram to mitigate the influence of ionospheric disturbs (Hu et al., 2012). The POT and MAI measurements have similar spatial resolution to the DInSAR measurements. The DInSAR, POT, and MAI measurements (Figures 2a–2h) were properly combined to calculate the cumulative three-dimensional (3-D) coseismic displacement field (Figures 2i–2k) using the improved strain model and variance component estimation method (J. Liu, Hu, et al., 2019).

## 2.2. Optical Images Processing

Sub-pixel correlation (SPC) of optical images provides useful information for the near-field displacement (e.g., Avouac et al., 2006; He, Feng, Feng, & Gao, 2019; Michel & Avouac, 2002; Socquet et al., 2019; Van Puymbroeck et al., 2000). The Planet-Lab optical imagery has a high spatial resolution (1–3 m) and short revisit cycle (1 day), as well as sufficient archived data (Planet Team, 2017), which will be helpful for separating the surface deformation of individual events in an earthquake sequence. In order to retrieve the 2-D horizontal coseismic displacement field of the 6 July mainshock, we cross-correlated the pre- and post-earthquake Planet-Lab image pair (04/07/2019–07/07/2019) that temporally covers only this event. We focused the optical data processing on the band 2 (~3 m resolution) of the Planet-Lab images (Feng et al., 2019), and cross-correlated them using the COSI-Corr software package (Leprince et al., 2007). We set the sliding window size as  $32 \times 32$  pixels, the step size as 10 pixels (~30 m resolution), and the robustness iteration as 4 times.

The raw 2-D horizontal displacement field of the mainshock is shown in Figures 3a and 3b. This displacement field is divided into multiple adjacent rectangular blocks with different ramp patterns. A conventional method to remove the ramps is based on a linear fitting model after masking the near-field coseismic displacement region (He, Feng, Li, et al., 2019). However, we cannot accurately identify the coseismic displacement signals in the raw displacement maps due to the influence of the long wave-length ramps in each image block.

In order to get an accurate Planet-Lab 2-D horizontal displacement, we improved the long wavelength orbital ramp correction method proposed by Feng et al. (2019). Here we take the raw Planet-Lab N-S horizontal coseismic displacement component of the 6 July mainshock as an example, to show the procedure of correcting the long wavelength orbital ramp in the displacement field (Figure S7 in Supporting Information S1). First, we clip the N-S component of the InSAR-derived 3-D displacement field (Figure 2j) to the size of the raw Planet N-S displacement field (Figure 3b). Next, we outline the main deformed area near the rupture in the clipped N-S displacement field and mask the outlined area in the raw Planet N-S displacement field. Then, we use a polynomial curve fitting method to determine the long wavelength orbital ramp of each block by the unmasked area in the block. After that, we remove the long wavelength orbital ramp in each block from the raw Planet N-S displacement field. Finally, we perform a 7-by-7 median filter to reduce the noise (Figures 3i and 3j).

We utilized the same methods and parameter settings to process another Planet-Lab image pair (01/07/2019–04/07/2019) that temporally covers only the 4 July foreshock, to map the coseismic ground deformation (Figures 3k

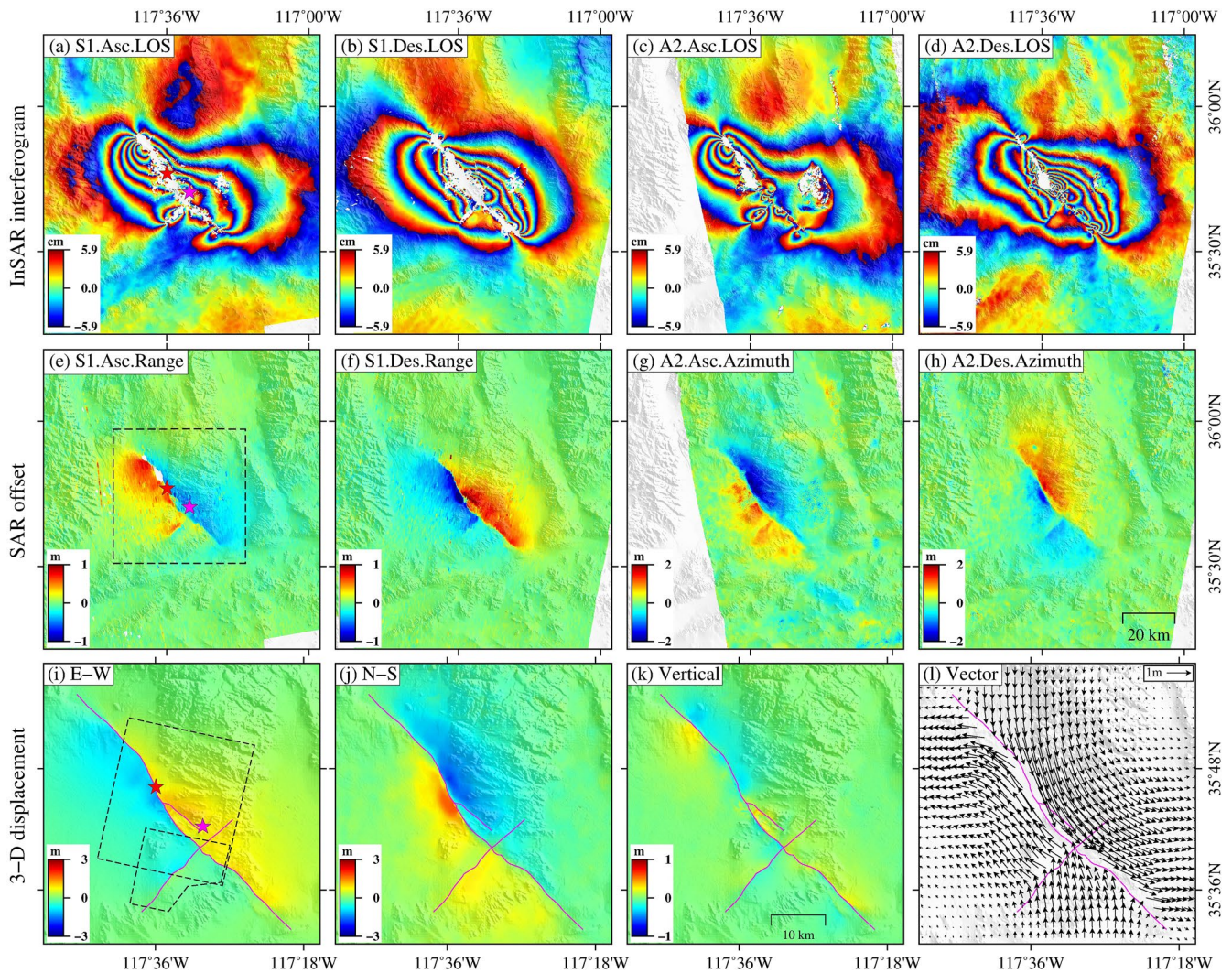


**Figure 2.** Coseismic displacement fields of the 2019 Ridgecrest earthquake sequence. (a) and (b) are the cumulative ascending and descending coseismic interferograms from Sentinel-1 images, respectively. (c) and (d) are the cumulative ascending and descending coseismic interferograms from Advanced Land Observing Satellite 2 (ALOS-2) images, respectively. (e) and (f) show the cumulative ascending and descending coseismic pixel offset-tracking range offsets from Sentinel-1 images, respectively. (g) and (h) are the cumulative ascending and descending coseismic multiple aperture interferometric synthetic aperture radar azimuth offsets from ALOS-2 images, respectively. (i)–(l) indicates the E-W, N-S, and vertical components of the 3-D cumulative surface displacement and the horizontal offset vectors (black arrows), respectively. Black dashed boxes in (e) and (i) denote the regions shown in (i)–(l) and Figure 3, respectively. Magenta lines depict the three fault segments used in the joint-event inversion. Different color tables are used in (a)–(l).

and 3l). There are only two GPS sites (named CLC and 5419) located in the Planet-Lab displacement field of the mainshock (Figure 3i), and no GPS site located in the Planet-Lab displacement field of the foreshock. In order to quantitatively assess the accuracy of the derived deformation maps, we calculated the root mean square error (RMSE) between the Planet-Lab and GPS data (Table S1 in Supporting Information S1) at the two GPS sites.

### 2.3. Coseismic Displacement Results

The cumulative 3-D coseismic displacement shows a complex ground deformation pattern. Around the mainshock hypocenter, the E-W displacement component is smaller than the N-S component (Figures 2i and 2j). The vertical motion is larger in the northern part of the mainshock rupture than in the southern part (Figure 2k). In the northern part, the east side subsided  $\sim 50$  cm, and the west side uplifted  $\sim 30$  cm. In the southern part, the east side experienced slight uplift ( $\sim 15$  cm), and the west side subsided slightly ( $\sim 10$  cm). As shown in Figure 2, the region on the east side of the mainshock rupture moves toward the south, then gradually rotates its strike to the

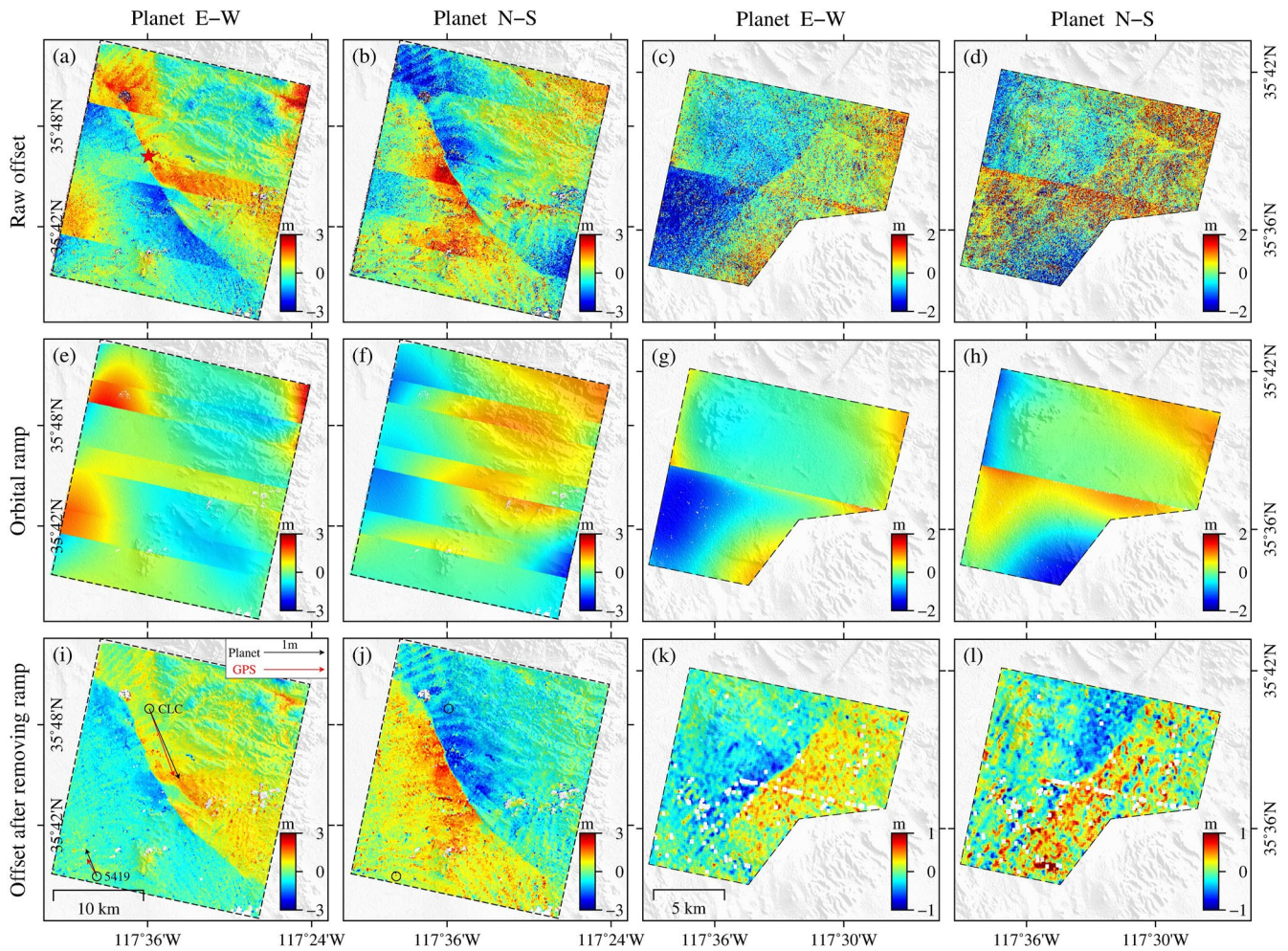


**Figure 3.** (a)–(d) Raw Planet-Lab horizontal offsets, (e)–(h) orbital ramps and (i)–(l) offsets after removing orbital ramps. Coseismic displacements in (a)–(b) and (c)–(d) temporally cover only the  $M_w$  7.1 event and only the  $M_w$  6.4 event, respectively. The location of the global positioning system (GPS) stations (named CLC and 5419) is marked by black circles in (i). The comparison of horizontal displacement between the Planet-Lab (black arrows) and GPS (red arrows) results are shown in (i). Different color tables are used in (a)–(l).

direction that is basically parallel to the SE-trending rupture, and finally moves toward the east. On the contrary, the region on the west side moves northward, then gradually rotates its strike to the direction that is almost parallel to the NW-trending rupture, and finally moves westward. As a whole, the 3-D displacement results suggest that the 2019 Ridgecrest earthquake sequence is dominated by a right-lateral motion.

The 2-D horizontal coseismic displacement spanning only the 6 July mainshock shows that a significant NW-SE-trending surface rupture occurred during the mainshock (Figures 3i and 3j). The E-W displacement map shows an eastward motion in the eastern part of the rupture and a westward motion in the western part (Figure 3i). Meanwhile, the N-S displacement map shows southward and northward motions in the eastern and western parts, respectively (Figure 3j). This 2-D displacement pattern is characterized by a right-lateral movement. Statistical results show that the RMSEs of the obtained Planet-Lab 2-D horizontal displacement of the mainshock are 10.86 and 11.76 cm for the EW and NS components, respectively (Table S1 in Supporting Information S1). Similarly, the pattern of the 2-D horizontal displacement spanning only the 4 July foreshock indicates that this event is dominated by a left-lateral motion along the NE-SW-trending rupture (Figures 3k and 3l). In general, the 2-D coseismic displacements patterns show that the Ridgecrest earthquake sequence took place on the conjugated strike-slip faults where the ruptures reached the surface.

## 2.4. Noise Estimation

InSAR, GPS displacements as well as optical and SAR pixel offsets contain some spatially correlated noise. To weigh different datasets in source modeling (see Section 3.1) and analyze the uncertainties of the fault slip parameters (see Section 3.4.1), the noise characteristics should be quantified and estimated. One way to achieve this is to build the variance-covariance matrix for each dataset independently, to generate multiple sets of synthetic noises. The noises are then added to the original datasets. We used the noise-perturbed datasets to estimate multiple sets of slip model parameters by performing a series of linear optimizations, so as to determine the model slip parameter uncertainties (Sudhaus & Jönsson, 2009).

For InSAR measurements, the spatially correlated noise is mainly attributed to atmospheric phase delays associated with topography, vertical stratification, and turbulent mixing (Hanssen, 2001). We empirically computed the semi-variograms and covariograms in the non-deforming field of the interferograms (Sudhaus & Jönsson, 2009), which can be used to estimate the variance and covariance of the InSAR data noise. Furthermore, we used a covariance function to characterize the spatial structures and statistics of the InSAR data noise. We assumed that the spatially correlated noise is second-order stationary and isotropic. The second-order stationary assumption means that the noise statistics extracted in the non-deforming field have the same patterns with the nearby deforming field, or can represent that of the whole displacement field. The isotropic assumption means that the covariance between pairs of InSAR data points is only related to their distance, not position or direction.

For GPS measurements, the noises in the data have spatial correlation, but it is difficult to determine the exact correlation patterns (Wright et al., 2004). In addition, most GPS stations are many kilometers apart, which weakens the influence of spatial correlation. Here, we used the GPS data uncertainties given in data processing to describe the variances. We took these values as the diagonal elements of the variance-covariance matrix and set the rest non-diagonal elements to zero. We assumed no spatial correlation between pairs of GPS data points. Nevertheless, the covariance values in the data variance-covariance matrix can be estimated if some relevant information is provided.

For optical and SAR measurements, the second-order stationary assumption is not suitable, because the data noise in the non-deforming field cannot represent that of the whole displacement field. We applied a four-step approach presented by Jolivet et al. (2014) to calculate the data variance-covariance matrix for the optical and SAR pixel offsets independently. Step one, estimate the standard deviation (STD) for different datasets from the far field non-deforming zone or stable deforming zone. Step two, perform linear inversion using the STD weighted datasets. Step three, calculate the empirical semi-variograms and covariograms by the randomly sampled data residuals. Step four, construct the full data variance-covariance matrix using the best-fitting covariance function.

The empirical semi-variograms  $\hat{V}(h_c)$  and covariograms  $\hat{C}(h_c)$  are computed at distance  $h_c$  according to the following equations (Sudhaus & Jönsson, 2009)

$$\begin{cases} \hat{V}(h_c) = \frac{1}{2N} \sum_{\substack{i=1 \\ \|r_i - s_i\| \approx h_c}}^N [d(r_i) - d(s_i)]^2 \\ \hat{C}(h_c) = \sum_{\substack{i=1 \\ \|r_i - s_i\| \approx h_c}}^N d(r_i) \cdot d(s_i) \end{cases} \quad (1)$$

Where  $d(r_i)$  and  $d(s_i)$  are the data values at pixel locations  $r_i$  and  $s_i$ , respectively.  $N$  is the number of pixel pairs at  $r_i$  and  $s_i$  within a certain distance centered at  $h_c$ , such that  $\|r_i - s_i\| \approx h_c$ . We then use a 1-D exponential decay to fit the positive-definite covariance function of each dataset independently, which is expressed as  $C(h) = a \cdot e^{-h/b}$ . Where  $a$  and  $b$  are the unknown coefficients to be estimated and  $C(h)$  is the fitted covariance value at any given distance  $h$  (Figure 4). To calculate  $\hat{V}(h)$  and  $\hat{C}(h)$ , we set  $h$  ranging from 0.2 to 30 km and 0.02–3 km for the SAR data (Figures 4a and 4b) and optical horizontal offsets (Figure 4c), respectively. Statistical results indicate that the empirical semi-variogram values increase asymptotically to the sill variance value of data noise (Figure S8 in Supporting Information S1).

The best-fitted covariance functions and sill variances for the four InSAR interferograms, four SAR image offsets, and four Planet-Lab optical horizontal offsets are shown in Figure 4 and Table S2 in Supporting Information S1. For InSAR measurements, the spatially correlated length of the data noise is up to 25 km (Figure 4a), but the noise level is small. For SAR measurements, the correlation length in the S1 range offset (less than 5 km) is smaller than that in the ALOS-2 azimuth offset (up to 30 km; Figure 4b), and the sill variances of the former is

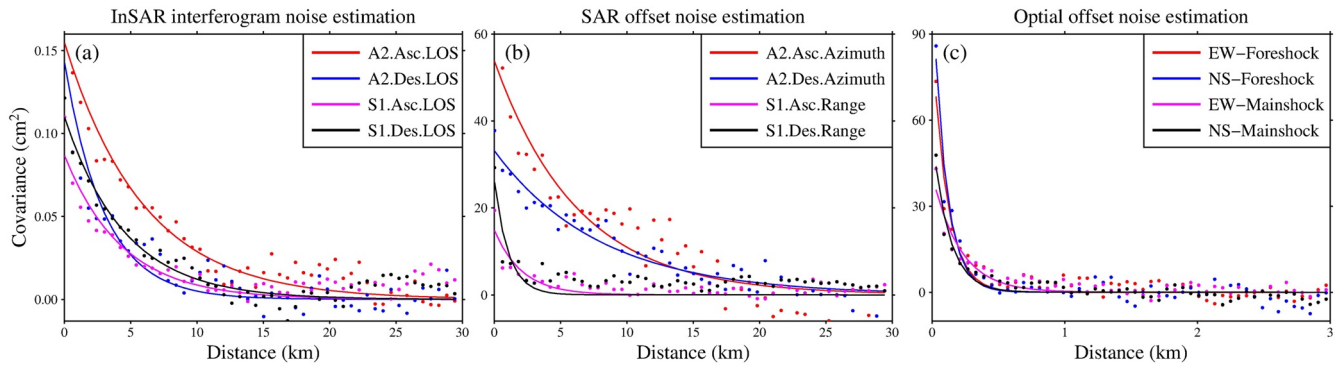


**Figure 4.** Data noise empirical covariograms (colored dots) and fitted covariance functions (colored lines) for the (a) interferometric synthetic aperture radar interferograms, (b) synthetic aperture radar and (c) optical image offsets.

also smaller (Table S2 in Supporting Information S1). This suggests that the data noises in the former are less spatially correlated than that in the latter. For optical measurements, the correlation length is close to 1 km in the EW component of the mainshock and about 0.5 km in the other three components (Figure 4c), which means that the data noise in the former has a higher spatial correlation than that in the latter three. In addition, the variances and covariances for the optical measurements are about three orders of magnitude higher than those for the InSAR measurements (Table S2 in Supporting Information S1), because the optical data have lower precision than the InSAR data.

### 3. Source Modeling and Inversion Strategy

#### 3.1. Data Downsampling and Weighting

Before source modeling, to reduce the computation load, the InSAR interferograms were downsampled by an algorithm that considers both fringe rate and coherence (Feng et al., 2010). The SAR and optical image offsets were downsampled using the quadtree algorithm (Jónsson et al., 2002), which maintains high spatial sampling in areas with high deformation gradients, and downsamples the data in areas with low deformation gradient. Before data downsampling, the geodetic observations with signal-to-noise ratio smaller than 0.9 and null values were masked.

We took the structure of the noise (see Section 2.4) into consideration to weigh the data by matrix  $\mathbf{W}$ . First, we used the covariance functions and sill variances of the data noise to build the full data variance-covariance matrix  $\Sigma_r$ . Next, the downsampled data variance-covariance matrix  $\Sigma_d$  were expressed as  $\Sigma_d = \mathbf{C} \Sigma_r \mathbf{C}^T$ , where  $\mathbf{C}$  is the operator relating the full data vector  $\mathbf{d}_f$  to the downsampled data vector  $\mathbf{d}$  by  $\mathbf{d}_f = \mathbf{C} \mathbf{d}$ . Then, on the basis of the matrix  $\mathbf{c}$ , we computed the weighting matrix  $\mathbf{W}$  by  $\Sigma_d^{-1} = \mathbf{W}^T \mathbf{W}$ .

#### 3.2. Inversion for Coseismic Slip Distribution

##### 3.2.1. Method

The coseismic slip distributions of the 4 July  $M_w$  6.4 foreshock and 6 July  $M_w$  7.1 mainshock are determined by inverting all available space geodetic data, including the InSAR, SAR, optical and GPS coseismic displacements, under the assumption that the seismic rupture is approximated by rectangular dislocations in an elastic, homogeneous and isotropic half-space domain (Okada, 1992).

We build four models in total (i.e., two single-event models, one joint-event model, and one combined-data model), each model is constrained by different data. The foreshock-only model is constrained by the Planet-Lab optical and GPS data that temporally cover only the foreshock. The mainshock-only model is constrained by the Planet-Lab optical and GPS data that temporally cover only the mainshock. The joint-event model is constrained by four SAR image offsets and four InSAR LOS displacements that temporally cover both earthquakes. The combined-data model is constrained by all the user data above. We use the first two models to individually separate the coseismic slip distribution of each event and the fourth model to simultaneously separate the coseismic

slip distribution of each event. We use the third model to simultaneously estimate the cumulative coseismic slip distribution of both events.

In source modeling, the fault geometry was constrained by the rupture trace at the surface mapped from the field investigation (Floyd et al., 2020) and the Planet-Lab image displacement field (Figure S6 in Supporting Information S1). A linear inversion was performed to estimate the fault slip distribution on rupture planes, using the fast non-negative constrained least square algorithm (Bro & De Jong, 1997). The second-order Laplace smoothing constraint was imposed among the adjacent slip patches to avoid fault slip abrupt changes (Jónsson et al., 2002). For the two single-event models and the joint-event model, the linear inverse problem is expressed as:

$$\begin{bmatrix} \mathbf{Wd} \\ \mathbf{0} \end{bmatrix} = \begin{bmatrix} \mathbf{Wd} \\ \kappa \mathbf{D} \end{bmatrix} \mathbf{m} \quad (2)$$

Where  $\mathbf{W}$  is the data weighting matrix (see Section 3.1).  $\mathbf{d}$  is the vector of data observations.  $\mathbf{m}$  is the vector of model slip parameters (strike-slip and dip-slip values on each slip patch)  $\mathbf{G}$  is the Green's function matrix relating  $\mathbf{d}$  to  $\mathbf{m}$  is the smoothing factor selected from the trade-off curve between data root-mean-square (RMS) misfit and model roughness (Figure S3 in Supporting Information S1). We took the slip solutions of the joint-event model as an example to show some extreme slip models using different smoothing factors (Figure S4 in Supporting Information S1).  $\mathbf{D}$  is the smoothing operator used to characterize the correlations between slips on the neighboring slip patches (Jónsson et al., 2002). For the combined-data model, the linear inverse problem is defined as (e.g., Ragon et al., 2019):

$$\begin{bmatrix} \mathbf{Wd} \\ \mathbf{0} \\ \mathbf{0} \end{bmatrix} = \begin{bmatrix} \mathbf{W}\mathbf{G}^F & \mathbf{W}\mathbf{G}^M \\ \kappa_F \mathbf{D}^F & \mathbf{0} \\ \mathbf{0} & \kappa_M \mathbf{D}^M \end{bmatrix} \begin{bmatrix} \mathbf{m}^F \\ \mathbf{m}^M \end{bmatrix} \quad (3)$$

Where  $\mathbf{G}^F$  and  $\mathbf{G}^M$ ,  $\mathbf{D}^F$  and  $\mathbf{D}^M$ ,  $\kappa_F$  and  $\kappa_M$ ,  $\mathbf{m}^F$  and  $\mathbf{m}^M$  are the Green's function matrices, smoothing operators, smoothing factors, and model slip parameters of the foreshock and the mainshock, respectively. Detailed expressions of  $\mathbf{d}$ ,  $\mathbf{G}$  and  $\mathbf{m}$  are given in Section 3.2.5. The fault segment optimization strategies for different models are described as below.

### 3.2.2. Foreshock Model Constrained by Planet-Lab and GPS Data

We determined the coseismic slip distribution of the 4 July foreshock using the Planet-Lab offsets (Figures 3k and 3l) and 41 GPS observations (Figure S1 in Supporting Information S1). As suggested by the early aftershock distribution and epicentral location of the foreshock (Figure 1b), there may be two perpendicular fault segments ruptured after this event (Barnhart et al., 2019), but the NW-trending fault segment is hard to identify in the Planet-Lab image displacement field (Figures 3k and 3l). For simplicity, we chose a NE-trending fault segment with variable strikes (marked as F3 in Figure 5b) to approximate the seismogenic fault of this event. We further discretized segment F3 into an array of 1.5 km by 1.5 km rectangular slip patches along-strike and -dip directions, respectively. The length and depth of segment F3 were extended into 21 and 12 km, respectively.

On the basis of the focal mechanism solution given by U.S. Geological Survey (2019a), we carried out an initial inversion to determine the optimal fault dip. We used the rectangular dislocation model to compute Green's function and to simulate the coseismic displacement. We set the dip angle of segment F3 varying between 70°E and 70°W with a step of 1° and adjusted the parameters by the trial-and-error tests to minimize the RMS misfit between the observed and the modeled coseismic displacements. All tests favor the segment with a ~86° westward-dipping geometry (Figure S3f in Supporting Information S1), which is consistent with the results of Barnhart et al. (2019) and Ross et al. (2019). On this basis, we estimated the detailed coseismic fault slip distribution. The EW and NS components of the 41 GPS observations were used in the inversion (Figure 6a), but their vertical components were not used due to their large uncertainties.

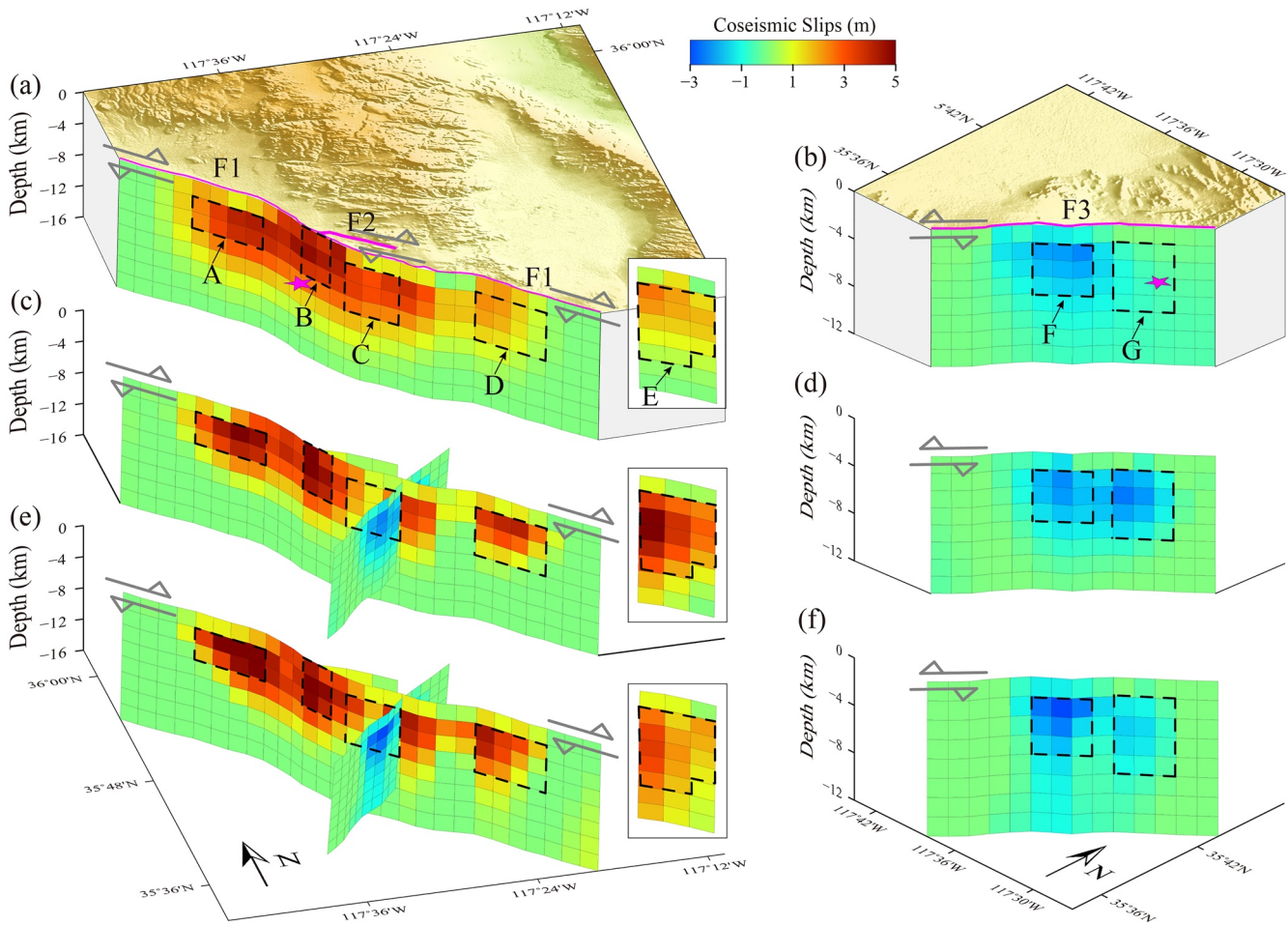


**Figure 5.** Top view of the coseismic slip distributions along the surface ruptures. (a) and (b) show the coseismic fault slip distributions of the mainshock-only and the foreshock-only models, respectively. The magenta stars indicate the epicentral locations of relevant events. (c) and (e) show the coseismic fault slip distributions of the joint-event and the combined-data models, respectively. Insets in (a), (c), and (e) show the slip component on segment F2 of relevant slip models. (d) and (f) represent the slip component on segment F3 in (c) and (e), respectively. Zones A-E in (a) and zones F-G in (b) show the major coseismic slip differences among different slip models. The fault planes of the mainshock and the foreshock are viewed at a 30° depression angle from the southwest and the southeast directions, respectively.

### 3.2.3. Mainshock Model Constrained by Planet-Lab and GPS Data

The Planet-Lab offsets (Figures 3i and 3j) and 38 GPS observations (Figure S2 in Supporting Information S1) were used for the source modeling of the July 6 mainshock. The Planet-Lab data have good coverage in the epicentral region, but insufficient coverage at the two ends of the seismogenic fault in the time span from 4 July to 7 July. Fortunately, there are some GPS stations located close to the two ends of the fault. The field investigation showed that the surface rupture is curved in the central section and has multiple small branches in the northern tip (Figure 1e), indicating that this event had a geometrically complex fault structure. For simplicity, we adopted two NW-SE-trending fault segments with variable strikes (marked as F1 and F2 in Figure 5a) to constrain the fault geometry, because they are clearly visible in the Planet-Lab image displacement field (Figures 3i and 3j).

We estimated the fault geometry of the mainshock by the scheme for the foreshock (see Section 3.2.2). We also set the dip angle of segments F1 and F2 varying between 70°E and 70°W with a step of 1°. The inversion results show that the mainshock-only model with two westward-dipping segments F1 (~88°W) and F2 (~88°W) can fit the geodetic data well (Figures S3d and S3e in Supporting Information S1), in agreement with the solution given by C. Liu, Lay, et al. (2019) and U.S. Geological Survey (2019b). We then extended the fault plane length of segments F1 and F2 to 56 and 6 km, respectively, and fixed the depth to 16 km. The fault planes were further divided into 2 km by 2 km square elements. Finally, we inverted the fault slip distribution on the basis of the fixed fault geometry.

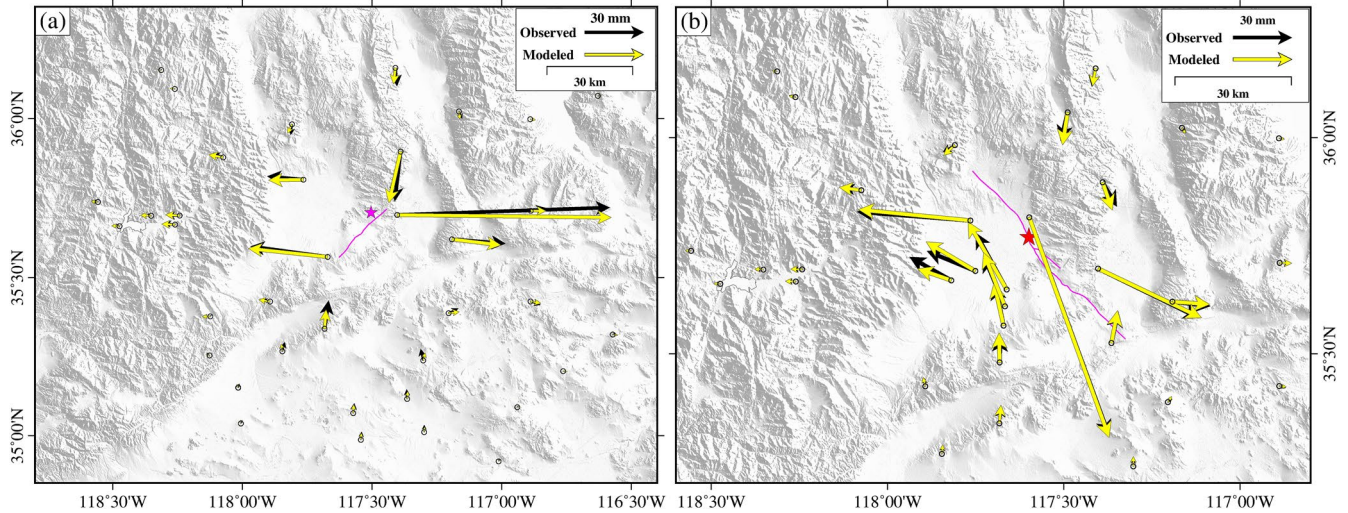


**Figure 6.** Observed (black arrows) and modeled (yellow arrows) horizontal displacements at global positioning system (GPS) sites that temporally cover only the (a) foreshock and only the (b) mainshock. The magenta lines are the fault traces used in relevant inversions. The magenta and red stars show the epicentral locations of the foreshock and the mainshock, respectively. The epicentral distances of the GPS stations used for inversion are less than 100 km.

### 3.2.4. Joint-Event Model Constrained by InSAR and SAR Data

For the joint inversion of both the 4 and 6 July events, we used the space-based geodetic data, including four InSAR interferograms (Figures 2a–2d) and four SAR image offsets (Figures 2e–2h), to estimate the coseismic slip distribution on the fault segments F1–F3. The joint inversion procedure is similar to that for the foreshock in Section 3.2.2. In order to compare the fault slip differences between the single-event and joint-event models, the fault geometry parameters used in the joint-event inversion are the same as those used in the two single-event inversions.

### 3.2.5. Combined-Data Model Constrained by Planet-Lab, GPS, InSAR, and SAR Data Sets

Different datasets bring different information for model inversion. We thus built a model for the two earthquakes using the combination of all the used datasets, including InSAR LOS observations, GPS displacements, SAR, and optical image offsets, to simultaneously invert and separate the coseismic slip distribution of the individual events. This requires careful construction of the Green's function matrix in the linear inverse problem  $\mathbf{Wd} = \mathbf{WGm}$ , which can be written as:

$$\mathbf{d} = \begin{bmatrix} \mathbf{d}_{Opt}^F \\ \mathbf{d}_{GPS}^F \\ \mathbf{d}_{Opt}^M \\ \mathbf{d}_{GPS}^M \\ \mathbf{d}_{SAR}^{FM} \\ \mathbf{d}_{InSAR}^{FM} \end{bmatrix} \mathbf{G} = \begin{bmatrix} \mathbf{G}_{Opt}^F & \mathbf{0} \\ \mathbf{G}_{GPS}^F & \mathbf{0} \\ \mathbf{0} & \mathbf{G}_{Opt}^M \\ \mathbf{0} & \mathbf{G}_{GPS}^M \\ \mathbf{G}_{SAR}^{FM} & \mathbf{G}_{SAR}^M \\ \mathbf{G}_{InSAR}^{FM} & \mathbf{G}_{InSAR}^M \end{bmatrix} \mathbf{m} = \begin{bmatrix} \mathbf{m}^F \\ \mathbf{m}^M \end{bmatrix} \quad (4)$$

Where data vector  $\mathbf{d}$  is ordered as Planet-Lab optical and GPS 2-D horizontal coseismic displacements caused by the 4 July foreshock, Planet-Lab optical and GPS 2-D horizontal coseismic displacements caused by the 6 July mainshock, and four SAR offsets and four InSAR LOS cumulative coseismic displacements caused by both events.  $\mathbf{m}^F$  and  $\mathbf{m}^M$  are the coseismic slip parameters of the foreshock and the mainshock, respectively. The Green's function matrix  $\mathbf{G}$  relates  $\mathbf{d}$  to  $\mathbf{m}$  of relevant events. We separately created Green's function matrices for the optical and GPS datasets that spanned only the foreshock and only the mainshock, and for the SAR offsets and

**Table 2**  
Geodetic Moment Information of Each Fault Segment

Model	Single-event model				Joint-event model				
	Foreshock	Mainshock			Foreshock	Mainshock			
Event	F3	F1	F2	Total	F3	F1	F2	Total	Total
$M_0$ (N·m)	$5.15 \times 10^{18}$	$3.92 \times 10^{19}$	$5.40 \times 10^{18}$	$4.46 \times 10^{19}$	$6.38 \times 10^{18}$	$4.01 \times 10^{19}$	$8.86 \times 10^{18}$	$4.89 \times 10^{19}$	$5.53 \times 10^{19}$
$M_w$	6.44	7.03	6.46	7.07	6.50	7.04	6.60	7.09	7.12

InSAR interferograms datasets that spanned both events. We then assembled these matrices to form a complete **G** matrix. In the combined-data inversion, we used the fault segment optimization strategy that is the same as in the two single-event inversions (see Sections 3.2.2 and 3.2.3).

### 3.3. Inversion Results

#### 3.3.1. Coseismic Slip of Different Models

The geodetic moment and magnitude estimated by each slip model are listed in Table 2, and the coseismic slip distributions are shown in Figure 5. The best-fitting foreshock-only coseismic slip model shows that the coseismic slip is mainly distributed in the shallow depths between 2 and 8 km, with a peak slip value of  $\sim 2.5$  m in zone F of segment F3 at 4 km depth (Figure 5b). No significant slip can be seen in zone G. This event occurred on a NE-SW-trending and westward-dipping ( $\sim 86^\circ$ ) fault plane with an almost purely left-lateral strike-slip movement, which released the geodetic moment of  $5.15 \times 10^{18}$  N·m, leading to a moment magnitude of  $M_w$  6.44 earthquake (assuming the shear modulus of 32 GPa; Table 2). The foreshock-only model fits well with both the GPS (Figure 6a) and the Planet-Lab (Figures 7g and 7h) displacements.

The best-fitting foreshock-only coseismic slip model shows that most slips are concentrated in the upper crust between 0 and 10 km depth (Figure 5a). These slips are almost purely right-lateral strike-slips along the fault segments F1 and F2. Segment F1 is dipping at  $\sim 88^\circ$  toward the west, and its maximum slip is up to  $\sim 5$  m in zone B at a depth of 4 km. A slip of  $\sim 2$  m is seen in zone E of segment F2. The total geodetic moment of the two fault segments is  $4.46 \times 10^{19}$  N·m, equivalent to an  $M_w$  7.07 earthquake (Table 2). The best-fitting slip model can well recover the ground displacement characteristics of both the GPS (Figure 6b) and the Planet-Lab (Figures 7e and 7f) data.

The best-fitting joint-event coseismic joint slip model shows that the 2019 Ridgecrest earthquake sequence is predominated by right-lateral strike-slip faulting and accompanied by some left-lateral strike-slip motions (Figure 5c). The maximum right-lateral strike-slip of  $\sim 5.5$  m occurred in zone B of segment F1 at a shallow depth of 4 km. No obvious slip component is found in zone C of segment F1. A slip of  $\sim 3.5$  m is observed in zone D of segment F1. A right-lateral strike-slip of  $\sim 4.5$  m is seen in zone E of segment F2 at 6 km depth. Segment F3 experiences a left-lateral strike-slip motion with a maximum slip value of  $\sim 3$  m in zone G at 6 km depth. Our preferred joint-event model shows a geodetic moment  $5.53 \times 10^{19}$  N·m, corresponding to that of an  $M_w$  7.12 earthquake (Table 2). Both the InSAR interferograms (Figure 8) and the SAR image offsets (Figure S5 in Supporting Information S1) are well predicted by the best-fitting model. No conspicuous residual fringes and offsets can be seen in the vicinity of the earthquake area.

#### 3.3.2. Comparison Among Different Slip Models

Our inversion results show several important differences in the geodetic moment and slip amplitude on rupture planes between the single-event slip models and the joint-event slip model. Firstly, the geodetic moment on segment F3 estimated by the joint-event model is  $6.38 \times 10^{18}$  N·m ( $M_w$  6.5), about 19% larger than that estimated by the foreshock-only model ( $5.15 \times 10^{18}$  N·m;  $M_w$  6.44; Table 2). The possible reason is that a part of the slip component in zone C of segment F1 might be mapped into segment F3 during the joint-event inversion, resulting in no obvious slip component in zone C (Figure 5c) but a slip value of  $\sim 3$  m in zone G (Figure 5d). However, no significant slip can be seen in zone G in the foreshock-only slip model (Figure 5b).

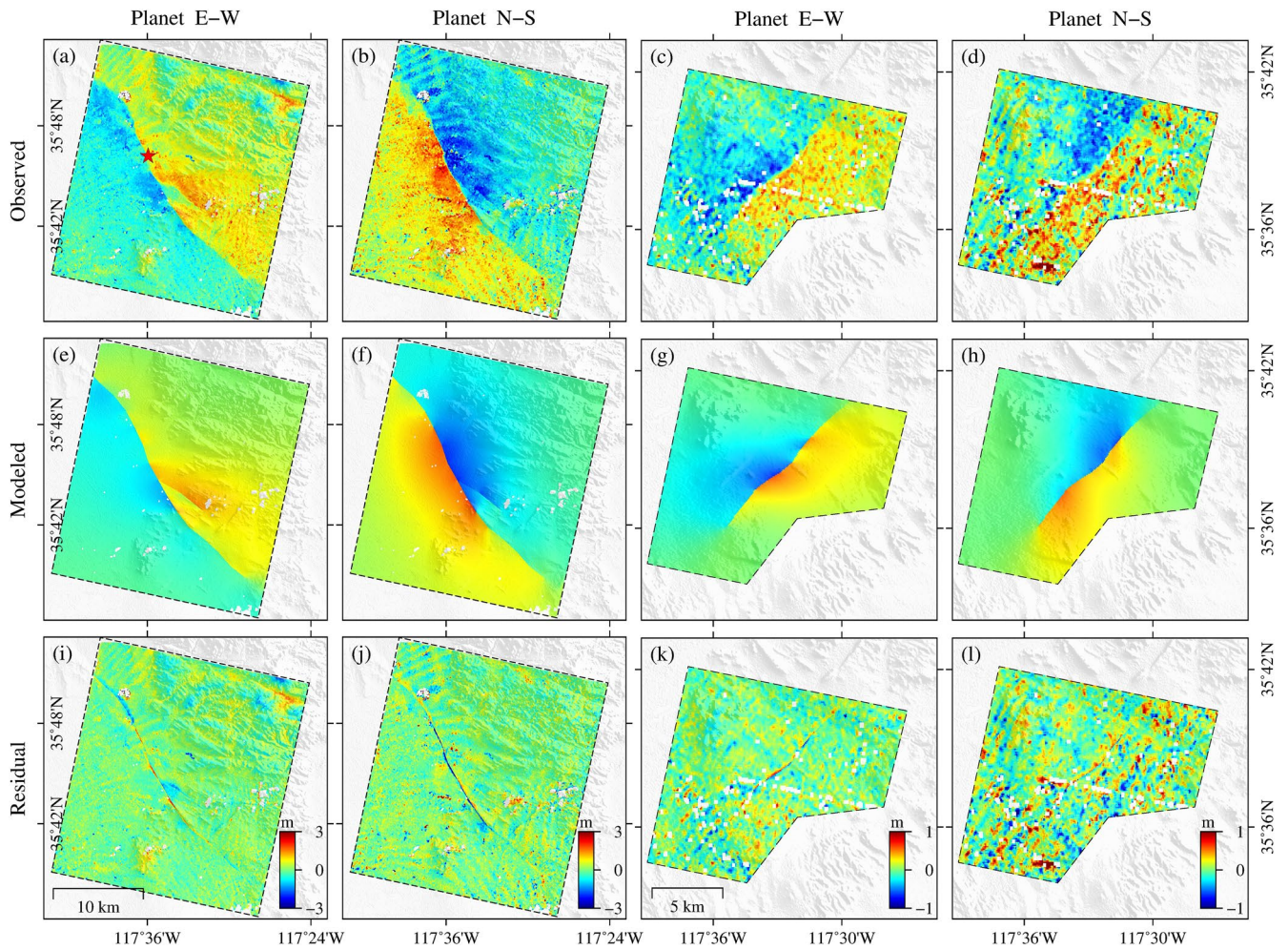


**Figure 7.** (a)–(d) Observed, (e)–(h) modeled, and (i)–(l) residual Planet-Lab 2-D horizontal offsets of the 2019 Ridgecrest earthquake sequence. The offsets in (e)–(f) and (g)–(h) are modeled by the mainshock-only slip model (Figure 5a) and the foreshock-only slip model (Figure 5b), respectively.

Secondly, the geodetic moment on segment F2 determined by the joint-event inversion is  $8.86 \times 10^{18}$  N·m ( $M_w$  6.60), almost 39% larger than that determined by the mainshock-only inversion ( $5.40 \times 10^{18}$  N·m;  $M_w$  6.46), because a part of slip component between zones A and B of segment F1 may be mapped into zone E, leading to a slip amplitude increases of up to  $\sim 4$  m in zone E in the joint-event slip model (Figure 5c), almost twice that ( $\sim 2$  m) in the mainshock-only slip model (Figure 5a).

Thirdly, the total geodetic moment on segments F1 and F2 derived by the joint-event inversion is  $4.89 \times 10^{19}$  N·m ( $M_w$  7.09), approximately 9% larger than that derived by the mainshock-only inversion ( $4.46 \times 10^{19}$  N·m;  $M_w$  7.07). This discrepancy may be related to the post-seismic deformation and aftershocks. The SAR data used to constrain the joint-event model spanned about 2–17 days after the mainshock (Table 1), while the Planet-Lab imagery used to constrain the mainshock-only model spanned only about 1 day after the mainshock.

Additionally, in the joint-event slip model, the slip distribution on segment F1 shows that the three main slip zones A–C are separated by slip patches with low amplitudes (Figure 5c), but they are connected to each other in the mainshock-only slip model (Figure 5a). In zone D, the slip amplitude in the latter model is smaller than that in the former one, perhaps due to the insufficient Planet-Lab data constraints in that zone. All these differences suggest that the slip pattern got by the joint-event model is rougher than that got by the single-event models, but it has a more concentrated slip distribution and larger slip amplitude in some zones on the rupture planes.

Finally, the combined-data slip model of both events is shown in Figure 5e. The main fault slip zones ruptured at shallow depths of 0–10 km. Compared with the joint-event slip model (Figure 5c), the slip magnitude in the

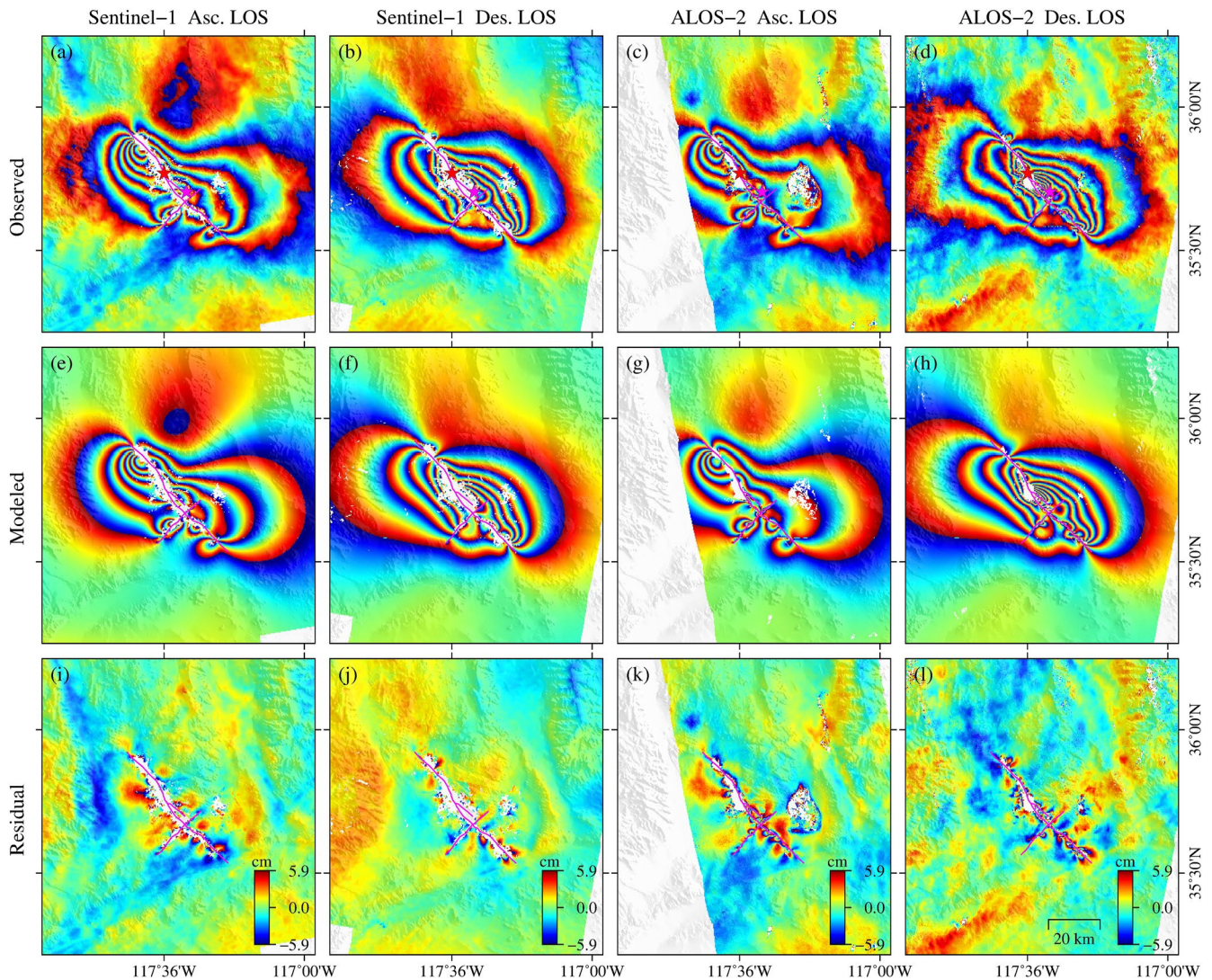


**Figure 8.** (a)–(d) Observed, (e)–(h) modeled and (i)–(l) residual interferograms of the 2019 Ridgecrest earthquake sequence. The interferograms in (e)–(h) are modeled by the best-fitting joint-event slip model (Figure 5c).

combined-data slip model is larger in zones A, D, and F but smaller in zones E and G (Figure 5e). In the combined-data slip model, most fault slips on segment F3 are mainly concentrated in zone F and no significant slip is seen in zone G (Figure 5f). A similar slip pattern is found in the foreshock-only slip model (Figure 5b). This suggests that the Planet-Lab optical data can be used to separate the seismic slip distributions of the individual events in the Ridgecrest earthquake sequence.

### 3.4. Analysis

#### 3.4.1. Uncertainty Analysis

On the basis of the covariance function of each dataset (Table S2 in Supporting Information S1), we simulated 100 sets of Gaussian random noises with zero mean using the Monte Carlo simulation approach. We then added these synthetic noises  $\epsilon_{synthi}$  to the predicted data vector  $\mathbf{d}_{pre}$  of the surface displacements to generate 100 sets of noise-perturbed data vectors  $\mathbf{d}_p$ , which are further used to repeat the inversion 100 times and estimate the uncertainties of the slip model parameters. The slip uncertainty on each patch was expressed as the STD of the slip parameter on that patch estimated by 100 repeated inversions. The linear equation for solving the model parameters  $\mathbf{m}_i$  is described by Sudhaus and Sigurjón (2009):

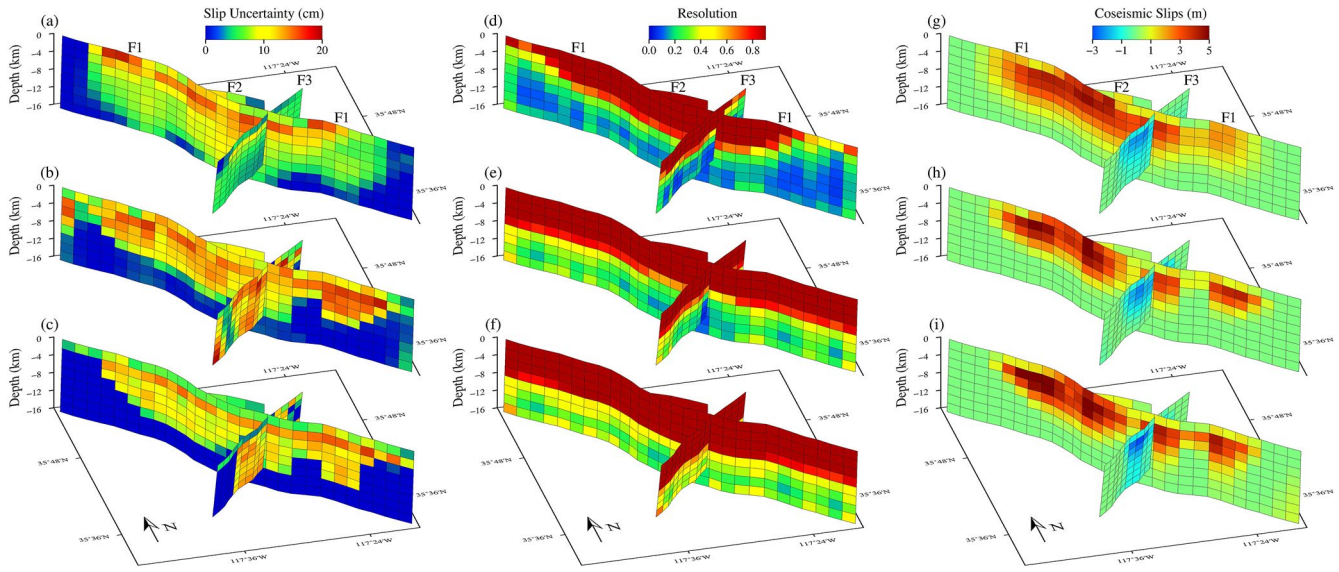


**Figure 9.** (Left column) Slip uncertainty, (middle column) resolution, and (right column) coseismic slip distribution of the (upper row) two single-event models, the (middle row) joint-event model and the (lower row) combined-data model. (a) shows the slip uncertainty on segments F1–F2 of the mainshock-only model and that on segment F3 of the foreshock-only model. (d) and (g) are the same as (a), but for resolution and coseismic slip, respectively.

$$\begin{bmatrix} \mathbf{d}_{pre} + \varepsilon_{synth,i} \\ \mathbf{0} \end{bmatrix} = \begin{bmatrix} \mathbf{G}_i \\ \kappa \mathbf{D} \end{bmatrix} \mathbf{m}_i \quad (i = 1, \dots, N) \quad (5)$$

Where  $\mathbf{G}_i$  is the Green's function matrix relating to the noise-perturbed data vector  $\mathbf{d}_i$ .  $\kappa$  is the smoothing factor.  $\mathbf{D}$  is the smoothing operator.

The slip uncertainties for different models are shown in Figures 9a–9c. The slip uncertainties of the two single-event models are small (Figure 9a), except for the mainshock segment F1 near the surface. The slip uncertainty of the combined-data model (Figure 9c) is generally smaller than that of the joint-event model (Figure 9b), suggesting that the former has better robustness than the latter. The maximum slip uncertainty of these models is only a dozen of centimeters, which is smaller than the meter-scale fault slip value (Figures 9g–9i). It confirms that the data noise has little impact on the fault slip models, and the slip pattern and amplitude of the coseismic slip distribution are robust.

### 3.4.2. Resolution Analysis

We used a resolution operator to describe the ability of the data to constrain the slip parameters on each patch (e.g., Loveless & Meade, 2011). The resolution operator  $\mathbf{R}$  is given by (Atzori & Antonioli, 2011):

$$\mathbf{R} = \mathbf{G}^{-g} \cdot \mathbf{G} = \{ \mathbf{V} \mathbf{\Lambda}_d^{-1} \mathbf{U}^T \} \cdot \{ \mathbf{V} \mathbf{\Lambda}^{-1} \mathbf{U}^T \} \quad (6)$$

Where  $\mathbf{G}^{-g}$  is the generalized inverse matrix of Green's function matrix  $\mathbf{G}$ .  $\mathbf{V}$  and  $\mathbf{U}$  are two unitary matrices.  $\mathbf{\Lambda}$  and  $\mathbf{\Lambda}_d^{-1}$  are the diagonal matrices filled with singular values  $\lambda$  and  $\lambda + \varepsilon^2$ , respectively.  $\varepsilon$  is a damping factor added to avoid too small singular values in the matrix  $\mathbf{\Lambda}$ , and it is determined by the trial-and-error test.  $\mathbf{R}$  is a diagonal matrix with a resolution between 0 and 1. Value 0 means that the slip parameter is unsolved, and 1 means that it is completely solved. We consider the cumulative sum of all elements in the relevant line of the matrix  $\mathbf{R}$  as the resolution value on each slip patch (Jolivet et al., 2012).

The resolution analysis shows that the two single-event inversions have to resolve power on the main slip patches (Figure 9d). Resolution is poor on the northeast end of segment F3 and the two ends of segment F1. The joint-event and the combined-data inversions have similar resolving power on most slip patches at the depth of 0–6 km,

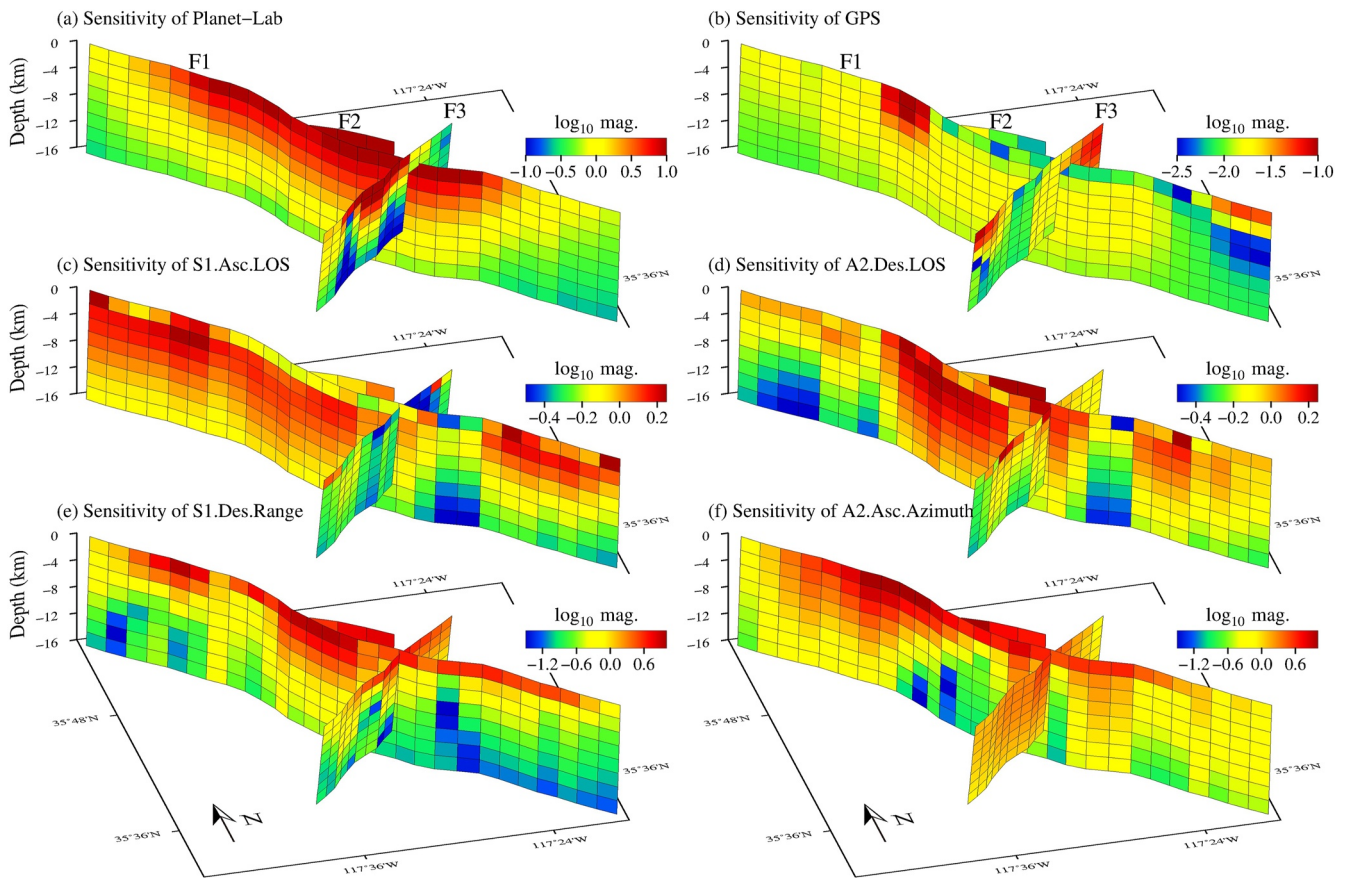


**Figure 10.** Sensitivity of (a) Planet-Lab data, (b) global positioning system observations, (c)–(d) interferometric synthetic aperture radar interferograms and (e)–(f) synthetic aperture radar image offsets. The sensitivity value is displayed in logarithmic form.

but the latter (Figure 9f) shows higher resolution than the former on fault patches at the depth of 6–8 km (Figure 9e). This suggests that the slip solution of the combined-data inversion is more constrained.

### 3.4.3. Sensitivity Analysis

We use a sensitivity operator to visualize the location where each dataset actually constrains slips (e.g., Loveless & Meade, 2011). This operator is computed by summing the surface displacement caused by unit slip on the individual patch. We express the sensitivity on the individual slip patch as the sum of all elements in the relevant line of the Green's function matrix  $\mathbf{G}$ . We estimated some representative sensitivity operators for InSAR, SAR, optical, and GPS datasets.

In the foreshock-only model, the fault slip on the central part and both sides of segment F3 are constrained by the Planet-Lab (Figure 10a) and GPS (Figure 10b) data, respectively. In the mainshock-only model, the fault slip on segment F1 is more constrained by the Planet-Lab data compared with the GPS data, because the large distance between the GPS stations limits the slip constraint. In the joint-event model, the sensitivity of the Sentinel-1 ascending LOS displacement is higher on the northwestern part of segment F1 (Figure 10c), which compensates for the lower sensitivity of ALOS-2 descending LOS displacement in this area (Figure 10d). On the southwestern part of segment F3, the higher sensitivity of the ALOS-2 ascending azimuth offset (Figure 10f) compensates for the lower sensitivity of the Sentinel-1 descending range offset (Figure 10e).

## 4. Discussion

### 4.1. Coseismic Slip Distribution Separated by Planet-Lab Imagery

The surface displacement of the earthquake sequence is sometimes hard to separate as multiple subevents usually occurred closely in time and space. In this study, we have separated the surface displacement of the two strongest subevents of the 2019 Ridgecrest earthquake sequence by the Planet-Lab imagery. Unlike push-broom optical satellites (e.g., Landsat-8 and Sentinel-2), multiple adjacent PlanetScope images with frame geometry are required in monitoring a wide range area like the 2019 Ridgecrest earthquakes. However, images acquired by adjacent satellites would lead to different long wavelength orbital ramp patterns. Here we use an improved error correction method (see Section 2.2) to remove the ramps of each image block instead of performing the linear regression fit for the whole image (Milliner & Donnellan, 2020). We utilize the 3-D displacement calculated by the multi-sight datasets (i.e., InSAR interferograms and SAR image offsets) to mask the near-field deformed area, and accurately correct the long wavelength artifacts of each Planet-Lab image block, which are determined from the far-field non-deformed areas in the block. Here the Planet-Lab imagery is used for the first time to separate the coseismic slip distribution of the  $M_w$  6.4 and  $M_w$  7.1 events. The estimated slip distributions reflect the main ground deformation features of the two quakes (Figures 7e–7h), benefitting from the near-field dense data constraints.

Comparison with the independent GPS measurements suggests that the RMSE of the derived Planet-Lab 2-D horizontal displacement of the mainshock are 10.86 and 11.76 cm for the EW and NS components, respectively (Table S1 in Supporting Information S1). Data noise estimation of these optical measurements shows that the sill variances are about 331 and 195 cm<sup>2</sup> for the horizontal displacement of the foreshock and the mainshock, respectively (Table S2 and Figure S8 in Supporting Information S1), which are smaller than the corresponding sill variances of about 400 and 225 cm<sup>2</sup> estimated by Milliner and Donnellan (2020). This confirms that our results have a lower noise level and higher precision than those obtained by Milliner and Donnellan (2020). Our study demonstrates the capability of the Planet-Lab imagery in distinguishing surface deformation and providing additional constraints for source modeling. Furthermore, the Planet-Lab data also have good potential in measuring river-ice and water velocities (Kääb et al., 2019), because of their frequent and comprehensive acquisitions. Nevertheless, optical imagery is susceptible to weather conditions and decorrelation noises. Therefore, in the case of a large ground deformation area and no external data assistance, it is still difficult to eliminate the linear ramps in the Planet-Lab image offset field.

It is general that several large individual events ( $M > 6$ ) occur during an earthquake sequence and cause additional casualties. Obtaining the ground deformation and coseismic fault slip as soon as possible is essential for seismic emergency rescue. The GPS data can be used for separating the surface deformation of an earthquake sequence if the time interval between two quakes is shorter than 1 day, such as the 1987 Superstition Hills sequence (Larsen et al., 1992). If the time interval is longer, such as the 1994–2004 Al Hoceima sequence (Akoglu et al., 2006), the 2010–2011 Canterbury sequence (Atzori et al., 2012), the InSAR data could be used to distinguish the surface deformation pattern and the fault slip distribution of each subevent. The Planet-Lab imagery can compensate for the insufficient spatial resolution of GPS and seismic waveform data and poor temporal resolution of InSAR data, and has been applied to some researches on earthquake deformation monitoring, such as the 2016  $M_w$  7.8 Kaikoura (Kääb et al., 2017) and the 2018  $M_w$  7.5 Palu (Bao et al., 2019) earthquakes. We should take advantage of the high spatiotemporal resolution Planet-Lab imagery to better manage seismic emergencies in such a geometrically complex fault system in the future.

### 4.2. Single-Event Models Versus Joint Models

The analysis results present in Section 3.4 indicate that the model inversions constrained by different types of datasets have different slip parameter uncertainties and resolving powers. Uncertainty analysis shows that the slip parameter uncertainty in the combined-data model (Figure 9c) is smaller than that in the joint-event model (Figure 9b), because the source modeling of the former contains the near-field Planet-Lab data constraints. The resolution analysis indicates that the mainshock-only model has a higher resolution in the central part of segment F1 but lower at both ends (Figure 9d), due to limited data coverage. At the depth 6–8 km, the resolution in the combined-data model (Figure 9f) is higher than that in the joint-event model (Figure 9e), thanks to the additional constraint of the dense Planet-Lab optical data in kinematic inversion. The uncertainty and resolution analysis results suggest that the combined-data inversion of InSAR, SAR, optical, and GPS datasets provides a more reliable

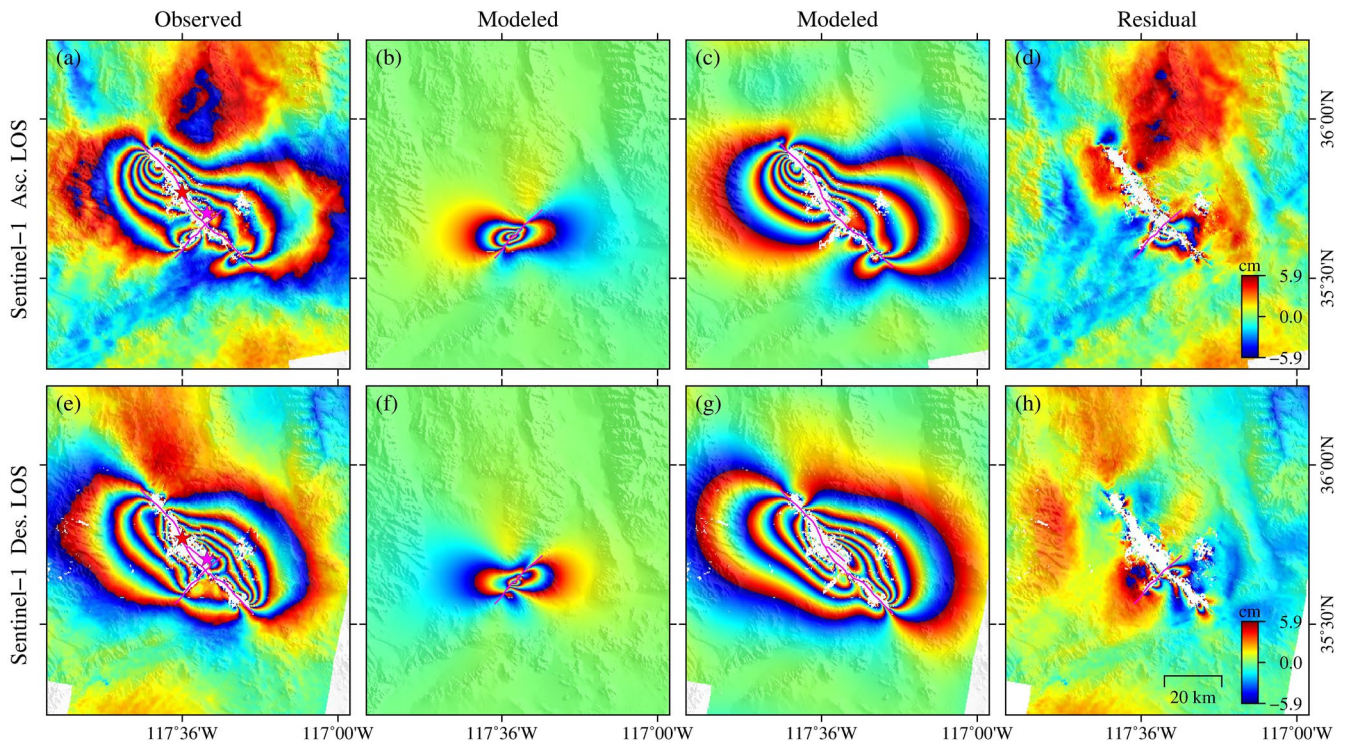


**Figure 11.** Observed, modeled, and residual interferograms of the 2019 Ridgecrest earthquake sequence. The interferograms in (b), (f), and (c), (g) are modeled by the best-fitting foreshock-only (Figure 5b) and mainshock-only (Figure 5a) slip models, respectively. (d) is the Sentinel-1 ascending line of sight (LOS) residual map after subtracting the modeled interferograms in (b) and (c) from the observed interferogram in (a). (h) is the same as (d), but shows the Sentinel-1 descending LOS residual map.

slip model (Figure 9i) with better robustness (Figure 9c) and higher resolving power (Figure 9f) for the two largest earthquakes in the Ridgecrest sequence. In addition, all models show a low resolution in the deeper fault patches (Figures 9d–9f). This does not mean that the slip solution in the fault zones is wrong, but means that the resolving power of the data is insufficient to obtain details of such level (Atzori & Antonioli, 2011).

There are some factors that affect the inversion results, such as the early postseismic deformation, the simplified fault geometry, and discretization. All the used datasets have different time spans and postseismic duration periods (Table 1) and may contain different proportions of early postseismic deformation. The Planet-Lab data only spanned about 1 day after the mainshock, so the effect of postseismic deformation could be small. The InSAR data spanned from 2 to 17 days after the mainshock. In order to estimate the postseismic deformation included in InSAR interferograms, we reproduce the ascending and descending Sentinel-1 InSAR interferograms related to the foreshock (Figures 11b and 11f) and the mainshock (Figures 11c and 11g) by single-event slip models. We then examine the possible contribution of cumulative postseismic deformation after removing the modeled deformation parts related to each event from the cumulative InSAR coseismic interferograms. The residual maps show several deformed fringes near the fault (Figures 11d and 11h). This pattern of postseismic deformation is consistent with the postseismic InSAR results presented by Wang and Bürgmann (2020), which showed centimeter-level cumulative postseismic displacement in a few months.

### 4.3. Comparison With Previous Coseismic Slip Models

The Planet-Lab imagery was mainly used for determining the surface rupture traces to constrain the fault geometry (e.g., Barnhart et al., 2019; Chen et al., 2020; Milliner & Donnellan, 2020), while the GPS data were mainly used for the fault slip inversion for the individual events (e.g., C. Liu et al., 2019; Li et al., 2020). C. Liu, Lay, et al. (2019) and S. Li et al. (2020) distinguished the coseismic slip distribution of the two subevents by inverting the GPS data and both constructed a cross-fault model for the foreshock. C. Liu, Lay, et al. (2019) stated that the foreshock was predominated by a left-lateral strike-slip motion on the NE-trending segment, while S. Li

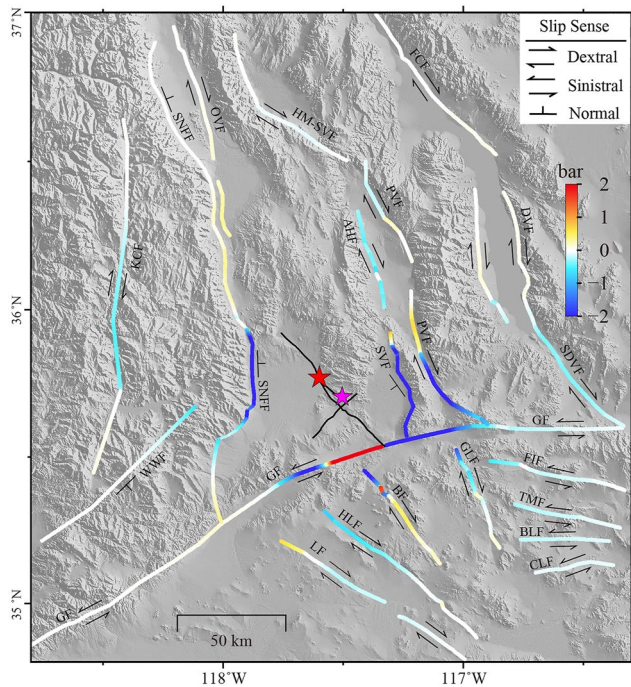


**Figure 12.** Coulomb failure stress changes on the surrounding active faults induced by the 2019 Ridgecrest earthquake sequence. The magenta and red stars are the epicentral locations of the 4 July  $M_w$  6.4 foreshock and 6 July  $M_w$  7.1 mainshock, respectively. The black lines are the fault traces used in the joint-event inversion. AHF = Ash Hill fault; BF = Blackwater fault; BLF = Bicycle Lake fault; CLF = Coyote Lake fault; DVF = Death Valley fault; FCF = Furnace Creek fault; FIF = Fort Irwin fault; GF = Garlock fault; GLF = Goldstone Lake fault; HLF = Harper Lake fault; HM-SVF = Hunter Mountain–Saline Valley fault; KCF = Kern Canyon fault; LF = Lockhart fault; OVF = Owens Valley fault; PVF = Panamint Valley fault; SDVF = southern Death Valley fault; SNFF = Sierra Nevada frontal fault; SVF = Saline Valley fault; TMF = Tiefert Mountain fault; WWF = White Wolf fault.

et al. (2020) believed that the right-lateral movement on the NW-trending segment was larger than the left-lateral movement on the NE-trending segment. We only utilized a single NE-trending fault segment F3 with a constant dip ( $86^\circ\text{W}$ ) to approximate the foreshock rupture plane (Figure 5b), because no significant orthogonal rupture was identified in the Planet-Lab image displacement field (Figures 3k and 3l). The foreshock-only model shows that this event is mainly controlled by a left-lateral motion, with a maximum slip value of  $\sim 2.5$  m at a shallow depth of 4 km (Figure 5b). The peak slip amplitude is larger than that determined by C. Liu, Lay, et al. (2019) and S. Li et al. (2020) models. These discrepancies may be related to different data constraints and fault geometries.

Researchers got different joint-event slip models (e.g., Barnhart et al., 2019; Chen et al., 2020; Feng et al., 2020; Pollitz et al., 2020; X. Xu et al., 2020), and their results were basically in agreement with ours, despite some differences in sliding details. In the northern segment of the mainshock fault, our best-fitting joint-event slip model yielded a better fit to the Sentinel-1 ascending interferogram (Figure 8e) than the model of Barnhart et al. (2019) did. This might be related to the different fault geometry of the westward-dipping segment in our model and the eastward-dipping segment in their model. The right-lateral strike-slip motion ( $\sim 3.5$  m) was clearly seen in zone D (Figure 5c), while it is inapparent in the model of Pollitz et al. (2020), perhaps because some near-field constraint data were removed in their inversion. Segment F2 was ruptured with a peak slip of up to  $\sim 4.5$  m according to the kinematic inversion results (Figure 5c), but it was not solved in the models of Barnhart et al. (2019), Chen et al. (2020), and Feng et al. (2020). In zone C, our joint-event model shows no obvious slip component (Figure 5c), which agrees with the result of X. Xu et al. (2020). By contrast, the fault slip in this zone was continuous in the model of Chen et al. (2020). Their model showed a slip amplitude larger than our model. This may be due to that our model considers the fault segments of both events in source modeling, while the fault geometry of their model only contains the fault plane of the mainshock.

#### 4.4. Regional Seismic Hazard Risk Evaluation

The regional stress changes caused by an earthquake can promote or delay the occurrence of seismic slip and seismicity on adjacent faults (e.g., He et al., 2021; King et al., 1994; Parsons et al., 2008). In order to evaluate the regional potential seismic risks, on the basis of the joint-event coseismic slip model (Figure 5c), we calculate the static CFS changes on the receiver faults surrounding the 2019 Ridgecrest earthquake sequence. The receiver faults consist of five sinistral strike-slip faults with nearly east–westward orientation, 12 dextral strike-slip faults with nearly northwest–southeastward orientation, and three normal faults with nearly north–southward orientation (Figure 12). The fault geometry of the receiver faults is modified from Frankel et al. (2008). According to Petersen et al. (2014), the dip angles of the strike-slip and normal receiver faults are set to  $90^\circ$  and  $50^\circ$ , respectively, for simplicity. The effective friction coefficient, Poisson's ratio, and shear modulus are assumed to be a typical value of 0.4, 0.25, and 32 GPa, respectively.

As shown in Figure 12, the increase in CFS changes mainly occurs on a  $\sim 30$  km long segment of the sinistral strike-slip Garlock fault (GF) near the southeast termination of the mainshock rupture, with a stress increase by up to  $>2$  bar. The GF reflects stress unloading in the east section of  $\sim 117.3^\circ\text{W}$  and the west section between  $117.6^\circ\text{W}$  and  $117.8^\circ\text{W}$ . The Sierra Nevada frontal fault (SNFF) shows a moderate stress increase of  $\sim 0.3$  bar in the north section between  $36^\circ\text{N}$  and  $36.4^\circ\text{N}$ , while its south section near the west of the mainshock epicenter experiences a significant CFS decrease ( $>2$  bar). In addition, the CFS changes on the southeastern Blackwater fault (BF), the southern Owens Valley fault (OVF), and the central Panamint Valley fault (PVF) have increased

by about 0.4–0.8 bar, which exceeds the earthquake triggering threshold of 0.1 bar (Hardebeck et al., 1998). This suggests that the potential seismic hazard risks on some nearby faults (GF, SNFF, BF, OVF, and PVF) may increase, so further attention should be paid to these faults.

#### 4.5. Limitations of the Elastic Homogeneity Hypothesis

Inverting geodetic data to solve for coseismic fault slip generally makes homogeneous elastic half-space assumption (Okada, 1992). It is useful in modeling the first order approximation of fault slip distribution but has limitations in representing the variable elastic properties of the shallow crust. If the approximated crust environment is different from the actual heterogeneous tectonic environment, simplifying the elastic structure of the medium into a homogeneous half-space or layered space may lead to underestimation or overestimation of the slip near the surface (e.g., Hearn & Bürgmann, 2005; Jolivet et al., 2015; Simons et al., 2002; C. Xu et al., 2010). Regional 3-D elastic structure plays an important role in evaluating the influence of elastic crust heterogeneity on the coseismic slip. Using the seismic velocities archived in a regional 3-D velocity model, Tung et al. (2021) simulated a 3-D elastic structure with spatially varying shear modulus in the surrounding area of the 2019 Ridgecrest earthquake sequence. They compared the LOS displacements of the seismogenic fault in the heterogeneous and the homogeneous elastic domains by the same amount of input slip. Their results indicated a non-uniform pattern of the displacement prediction differences.

We take the 4 July  $M_w$  6.4 foreshock as an example to estimate the coseismic slip solution by inverting both the Planet-Lab and GPS data using a layered elastic space model, which is assumed in a stratified semi-infinite elastic medium (e.g., Jolivet et al., 2015; Simons et al., 2002). Our layered-space model consists of three layers with different shear modulus and does not consider the possible lateral variations in elastic properties of the upper crust. The stratification of the shear modulus is modified from Simons et al. (2002). We compare the slip solution and moment of the layered-space model and the homogeneous half-space model. We find that the layered-space model with a longitudinally varying shear modulus can increase the slip magnitude by about 10%–20% (Figures 13c and 13e), compared with that estimated by the half-space model with a uniform shear modulus. Meanwhile, the geodetic moment is reduced about 23% from  $M_w$  6.50 ( $6.36 \times 10^{18}$  N·m) for the former model to  $M_w$  6.44 ( $5.15 \times 10^{18}$  N·m) for the latter. Similar solution differences have been modeled for other large strike-slip earthquakes, such as the 1999  $M_w$  7.1 Hector Mine (Simons et al., 2002), the 1999  $M_w$  7.4 Izmit (Hearn & Bürgmann, 2005), and the 2008  $M_w$  7.9 Wenchuan (C. Xu et al., 2010) earthquakes. They summarized that using a layered elastic structure in source modeling generally requires higher slip to fit the near-field geodetic data than using a homogeneous one.

## 5. Conclusions

In this study, we got an accurate Planet-Lab optical 2-D horizontal displacement fields for the 4 and 6 July Ridgecrest earthquakes using the improved long wavelength ramps correction method. The RMSE between the Planet-Lab data and GPS measurements are 10.86 and 11.76 cm for the EW and NS components, respectively. We inverted and separated the detailed coseismic slip distributions of the  $M_w$  6.4 foreshock and the  $M_w$  7.1 mainshock using the dense near-field Planet-Lab data and intermediate-field GPS data. The combination of InSAR, SAR, optical, and GPS datasets provides a powerful constraint on fault slip distribution for the two earthquakes. We show that using Planet-Lab data in the combined-data inversion can reduce the model slip parameter uncertainty and increase the model resolution, compared with the joint-event inversion constrained by InSAR and SAR data only. Our results suggest that the combined-data inversion can provide a more reliable slip model with better robustness and higher resolving power than the single-event and joint-event models. Some nearby faults have positive CFS changes induced by the 2019 Ridgecrest earthquake sequence, so the potential seismic hazards on the southeastern BF, the southern OVF, the central PVF, and the northern SNFF, especially on the central GF segment, deserve further attention.

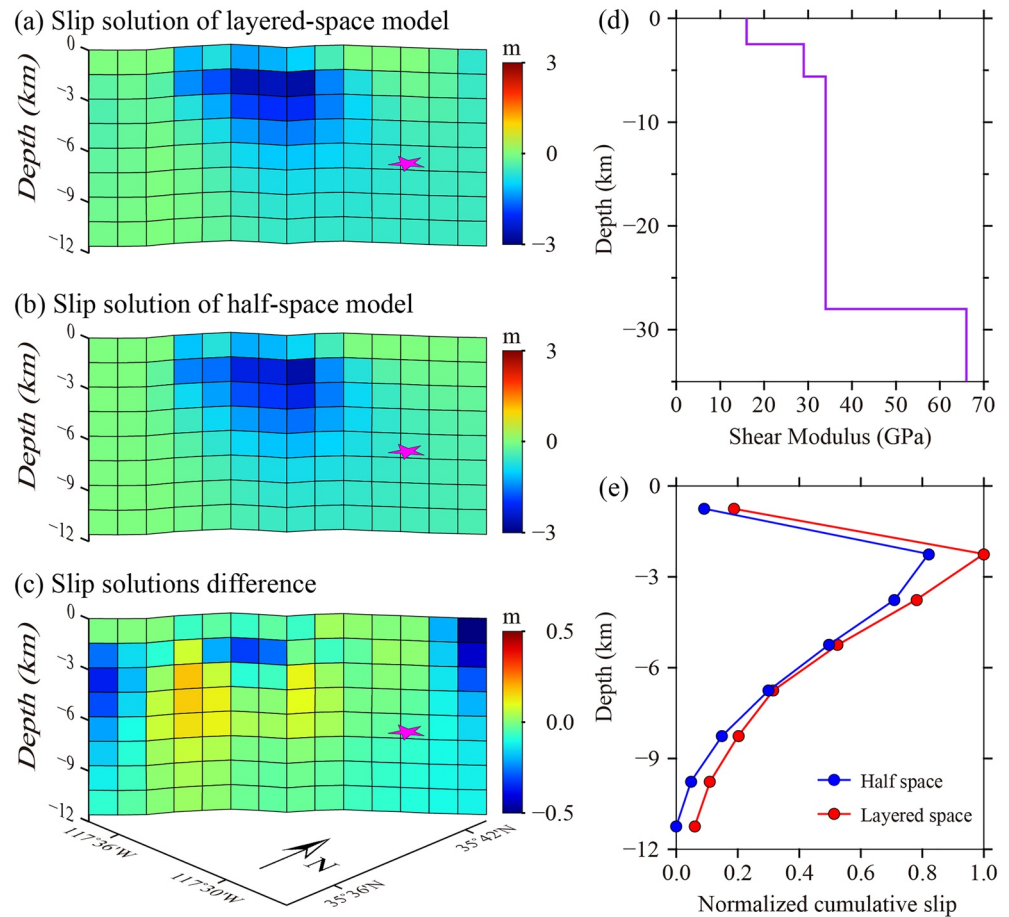


**Figure 13.** Coseismic slip solutions of the 4 July  $M_w$  6.4 foreshock using the (a) layered-space model and the (b) homogeneous half-space model, and the (c) slip magnitude difference between them. (d) Stratification of the shear modulus in the Eastern California Shear Zone was modified from Simons et al. (2002). (e) Normalized cumulative slip as a function of depth. Different color tables are used in (a)–(c).

### Data Availability Statement

The Sentinel-1 data are copyrighted by the European Space Agency (<http://scihub.copernicus.eu/dhus>) and additionally distributed by the Alaska Satellite Facility Distributed Active Archive Center (<https://vertex.daac.asf.alaska.edu>). The ALOS-2 data are provided by the Japan Aerospace Exploration Agency under Project ER3A2N043. The Planet-Lab data are not publicly accessed as Planet is a commercial company; however, scientific access schemes to these data exist (<https://www.planet.com/markets/education-and-research/>). The coseismic GPS observations are derived from the network of the UNAVCO Bulletin Board (<https://www.unavco.org/highlights/2019/ridgecrest.html>). The seismicity catalog used in this work is openly available at the network of the Southern California Earthquake Data Center ([http://service.scedc.caltech.edu/eq-catalogs/date\\_mag\\_loc.php](http://service.scedc.caltech.edu/eq-catalogs/date_mag_loc.php)).

### References

Akoglu, A. M., Cakir, Z., Meghraoui, M., Belabbes, S., El Alami, S. O., Ergintav, S., & Akyüz, H. S. (2006). The 1994–2004 Al Hoceima (Morocco) earthquake sequence: Conjugate fault ruptures deduced from InSAR. *Earth and Planetary Science Letters*, 252(3–4), 467–480. <https://doi.org/10.1016/j.epsl.2006.10.010>

Atzori, S., & Antonioli, A. (2011). Optimal fault resolution in geodetic inversion of coseismic data. *Geophysical Journal International*, 185(1), 529–538. <https://doi.org/10.1111/j.1365-246X.2011.04955.x>

Atzori, S., Tolomei, C., Antonioli, A., Merryman Boncori, J. P., Bannister, S., Trasatti, E., & Salvi, S. (2012). The 2010–2011 Canterbury, New Zealand, seismic sequence: Multiple source analysis from InSAR data and modeling. *Journal of Geophysical Research: Solid Earth*, 117(B8). <https://doi.org/10.1029/2012JB009178>

### Acknowledgments

We would like to thank the editor Isabelle Manighetti and an anonymous expert associate editor, the reviewers Romain Jolivet and Kejie Chen for their detailed and constructive comments that helped improve this work. We thank the European Space Agency for open access to Sentinel-1 data, the Japan Aerospace Exploration Agency for access to ALOS-2 data under Project ER3A2N043, the Planet Team (2017) for access to Planet-Lab optical imagery through an Academic and Research license, and the Nevada Geodetic Laboratory for providing GPS data. We acknowledge the COSI-Corr open-source software for optical data processing (<http://www.tectonics.caltech.edu>). The figures in the papers were generated by the Generic Mapping Tools (Wessel et al., 2013). This work was supported by the National Key R&D Program of China (No. 2018YFC1503603), the National Natural Science Foundation of China (No. 42174039), the Project of Innovation-Driven Plan of Central South University (No. 2019CX007), the Scientific Research Innovation Project for Graduate Students in Hunan Province (No. CX20210105), and the Fundamental Research Funds for the Central Universities of Central South University (No. 2021zzts0250).

- Avouac, J. P., Ayoub, F., Leprince, S., Konca, O., & Helmberger, D. V. (2006). The 2005, Mw 7.6 Kashmir earthquake: Sub-pixel correlation of ASTER images and seismic waveforms analysis. *Earth and Planetary Science Letters*, 249(3–4), 514–528. <https://doi.org/10.1016/j.epsl.2006.06.025>
- Bao, H., Ampuero, J. P., Meng, L., Fielding, E. J., Liang, C., Milliner, C. W., & Huang, H. (2019). Early and persistent supershear rupture of the 2018 magnitude 7.5 Palu earthquake. *Nature Geoscience*, 12(3), 200–205. <https://doi.org/10.1038/s41561-018-0297-z>
- Barnhart, W. D., Hayes, G. P., & Gold, R. D. (2019). The July 2019 Ridgecrest, California, earthquake sequence: Kinematics of slip and stressing in cross-fault ruptures. *Geophysical Research Letters*, 46(21), 11859–11867. <https://doi.org/10.1029/2019GL084741>
- Bechor, N. B., & Zebker, H. A. (2006). Measuring two-dimensional movements using a single InSAR pair. *Geophysical Research Letters*, 33(16). <https://doi.org/10.1029/2006GL026883>
- Bro, R., & De Jong, S. (1997). A fast non-negativity-constrained least squares algorithm. *Journal of Chemometrics: A Journal of the Chemometrics Society*, 11(5), 393–401. [https://doi.org/10.1002/\(SICI\)1099-128X\(199709/10\)11:5<393::AID-CEM483>3.0.CO;2-L](https://doi.org/10.1002/(SICI)1099-128X(199709/10)11:5<393::AID-CEM483>3.0.CO;2-L)
- Chen, C. W., & Zebker, H. A. (2002). Phase unwrapping for large SAR interferograms: Statistical segmentation and generalized network models. *IEEE Transactions on Geoscience and Remote Sensing*, 40(8), 1709–1719. <https://doi.org/10.1109/TGRS.2002.802453>
- Chen, K., Avouac, J. P., Aati, S., Milliner, C., Zheng, F., & Shi, C. (2020). Cascading and pulse-like ruptures during the 2019 Ridgecrest earthquakes in the eastern California shear zone. *Nature Communications*, 11(1), 1–8. <https://doi.org/10.1038/s41467-019-13750-w>
- Feng, G., Hetland, E. A., Ding, X., Li, Z., & Zhang, L. (2010). Coseismic fault slip of the 2008 Mw 7.9 Wenchuan earthquake estimated from InSAR and GPS measurements. *Geophysical Research Letters*, 37(1), L01302. <https://doi.org/10.1029/2009GL041213>
- Feng, W., Samsonov, S., Qiu, Q., Wang, Y., Zhang, P., Li, T., & Zheng, W. (2020). Orthogonal fault rupture and rapid postseismic deformation following 2019 Ridgecrest, California, earthquake sequence revealed from geodetic observations. *Geophysical Research Letters*, 47(5), e2019GL086888. <https://doi.org/10.1029/2019GL086888>
- Feng, Z., Feng, G., Chen, H., Xu, W., Li, Z., He, L., & Ren, Z. (2019). A block ramp errors correction method of Planet subpixel offset: Application to the 2018 Mw 7.5 Palu earthquake, Indonesia. *IEEE Access*, 7, 174924–174931. <https://doi.org/10.1109/ACCESS.2019.2956198>
- Floyd, M., Funning, G., Fialko, Y., Terry, R., & Herring, T. (2020). Survey and continuous GNSS in the vicinity of the July 2019 Ridgecrest earthquakes. *Seismological Research Letters*, 91(4), 2047–2054. <https://doi.org/10.1785/0220190324>
- Frankel, K. L., Glazner, A. F., Kirby, E., Monastero, F. C., Strane, M. D., Oskin, M. E., & Smith, E. I. (2008). Active tectonics of the eastern California shear zone. *Field guide to plutons, volcanoes, faults, reefs, dinosaurs, and possible glaciation in selected areas of Arizona, California, and Nevada* (Vol. 11, pp. 43–81). Geological Society of America Field Guide. [https://doi.org/10.1130/2008.fld011\(03\)](https://doi.org/10.1130/2008.fld011(03))
- Gabriel, A. K., Goldstein, R. M., & Zebker, H. A. (1989). Mapping small elevation changes over large areas: Differential radar interferometry. *Journal of Geophysical Research*, 94(B7), 9183–9191. <https://doi.org/10.1029/JB094iB07p09183>
- Goldberg, D. E., Melgar, D., Sahakian, V. J., Thomas, A. M., Xu, X., Crowell, B. W., & Geng, J. (2020). Complex rupture of an immature fault zone: A simultaneous kinematic model of the 2019 Ridgecrest, CA earthquakes. *Geophysical Research Letters*, 47(3), e2019GL086382. <https://doi.org/10.1029/2019GL086382>
- Hanssen, R. F. (2001). Radar interferometry. *Radar Interferometry: Data Interpretation and Error Analysis* (Vol. 2). Springer Science & Business Media. <https://doi.org/10.1007/0-306-47633-9>
- Hardebeck, J. L., Nazareth, J. J., & Hauksson, E. (1998). The static stress change triggering model: Constraints from two southern California aftershock sequences. *Journal of Geophysical Research*, 103(B10), 24427–24437. <https://doi.org/10.1029/98JB00573>
- He, L., Feng, G., Feng, Z., & Gao, H. (2019). Coseismic displacements of 2016 Mw 7.8 Kaikoura, New Zealand earthquake, using Sentinel-2 optical images. *Acta Geodaetica et Cartographica Sinica*, 48(3), 339. <https://doi.org/10.11947/j.AGCS.2019.20170671>
- He, L., Feng, G., Li, Z., Feng, Z., Gao, H., & Wu, X. (2019). Source parameters and slip distribution of the 2018 Mw 7.5 Palu, Indonesia earthquake estimated from space-based geodesy. *Tectonophysics*, 772, 228216. <https://doi.org/10.1016/j.tecto.2019.228216>
- He, L., Feng, G., Wu, X., Lu, H., Xu, W., Wang, Y., & Li, Z. (2021). Coseismic and early postseismic slip models of the 2021 Mw 7.4 Maduo earthquake (western China) estimated by space-based geodetic data. *Geophysical Research Letters*, 48(24), e2021GL095860. <https://doi.org/10.1029/2021GL095860>
- Hearn, E. H., & Bürgmann, R. (2005). The effect of elastic layering on inversions of GPS data for coseismic slip and resulting stress changes: Strike-slip earthquakes. *Bulletin of the Seismological Society of America*, 95(5), 1637–1653. <https://doi.org/10.1785/0120040158>
- Hu, J., Li, Z., Zhang, L., Ding, X., Zhu, J., Sun, Q., & Ding, W. (2012). Correcting ionospheric effects and monitoring two-dimensional displacement fields with multiple-aperture InSAR technology with application to the Yushu earthquake. *Science China Earth Sciences*, 55(12), 1961–1971. <https://doi.org/10.1007/s11430-012-4509-x>
- Jiang, G., Wen, Y., Liu, Y., Xu, X., Fang, L., Chen, G., & Xu, C. (2015). Joint analysis of the 2014 Kangding, southwest China, earthquake sequence with seismicity relocation and InSAR inversion. *Geophysical Research Letters*, 42(9), 3273–3281. <https://doi.org/10.1002/2015GL063750>
- Jin, Z., & Fialko, Y. (2020). Finite slip models of the 2019 Ridgecrest earthquake sequence constrained by space geodetic data and aftershock locations. *Bulletin of the Seismological Society of America*, 110(4), 1660–1679. <https://doi.org/10.1785/0120200060>
- Jolivet, R., Duputel, Z., Riel, B., Simons, M., Rivera, L., Minson, S. E., & Fielding, E. J. (2014). The 2013 Mw 7.7 Balochistan earthquake: Seismic potential of an accretionary wedge. *Bulletin of the Seismological Society of America*, 104(2), 1020–1030. <https://doi.org/10.1785/0120130313>
- Jolivet, R., Lasserre, C., Doin, M. P., Guillaso, S., Peltzer, G., Dailu, R., & Xu, X. (2012). Shallow creep on the Haiyuan fault (Gansu, China) revealed by SAR interferometry. *Journal of Geophysical Research: Solid Earth*, 117(B6). <https://doi.org/10.1029/2011JB008732>
- Jolivet, R., Simons, M., Agram, P. S., Duputel, Z., & Shen, Z. K. (2015). Aseismic slip and seismogenic coupling along the central San Andreas Fault. *Geophysical Research Letters*, 42(2), 297–306. <https://doi.org/10.1002/2014GL062222>
- Jónsson, S., Zebker, H., Segall, P., & Amelung, F. (2002). Fault slip distribution of the 1999 Mw 7.1 Hector Mine, California, earthquake, estimated from satellite radar and GPS measurements. *Bulletin of the Seismological Society of America*, 92(4), 1377–1389. <https://doi.org/10.1785/0120000922>
- Kääb, A., Altana, B., & Mascaro, J. (2017). Coseismic displacements of the 14 November 2016 Mw 7.8 Kaikoura, New Zealand, earthquake using the Planet optical cubesat constellation. *Natural Hazards and Earth System Sciences*, 17(5), 627–639. <https://doi.org/10.5194/nhess-17-627-2017>
- Kääb, A., Altana, B., & Mascaro, J. (2019). River-ice and water velocities using the Planet optical cubesat constellation. *Hydrology and Earth System Sciences*, 23(10), 4233–4247. <https://doi.org/10.5194/hess-23-4233-2019>
- King, G. C., Stein, R. S., & Lin, J. (1994). Static stress changes and the triggering of earthquakes. *Bulletin of the Seismological Society of America*, 84(3), 935–953. <https://doi.org/10.1785/BSSA0840030935>
- Konca, A. O., Avouac, J. P., Sladen, A., Meltzner, A. J., Sieh, K., Fang, P., & Helmberger, D. V. (2008). Partial rupture of a locked patch of the Sumatra megathrust during the 2007 earthquake sequence. *Nature*, 456(7222), 631–635. <https://doi.org/10.1038/nature07572>

- Larsen, S., Reilinger, R., Neugebauer, H., & Strange, W. (1992). Global Positioning System measurements of deformations associated with the 1987 Superstition Hills earthquake: Evidence for conjugate faulting. *Journal of Geophysical Research: Solid Earth*, 97(B4), 4885–4902. <https://doi.org/10.1029/92JB00128>
- Leprince, S., Barbot, S., Ayoub, F., & Avouac, J. P. (2007). Automatic and precise orthorectification, coregistration, and subpixel correlation of satellite images, application to ground deformation measurements. *IEEE Transactions on Geoscience and Remote Sensing*, 45(6), 1529–1558. <https://doi.org/10.1109/tgrs.2006.888937>
- Li, S., Chen, G., Tao, T., He, P., Ding, K., Zou, R., & Wang, Q. (2020). The 2019 Mw 6.4 and Mw 7.1 Ridgecrest earthquake sequence in eastern California: Rupture on a conjugate fault structure revealed by GPS and InSAR measurements. *Geophysical Journal International*, 221(3), 1651–1666. <https://doi.org/10.1093/gji/ggaa099>
- Li, Z. W., Ding, X. L., Huang, C., Zhu, J. J., & Chen, Y. L. (2008). Improved filtering parameter determination for the Goldstein radar interferogram filter. *ISPRS Journal of Photogrammetry and Remote Sensing*, 63(6), 621–634. <https://doi.org/10.1016/j.isprsjprs.2008.03.001>
- Liang, C., & Fielding, E. J. (2017). Measuring azimuth deformation with L-band ALOS-2 ScanSAR interferometry. *IEEE Transactions on Geoscience and Remote Sensing*, 55(5), 2725–2738. <https://doi.org/10.1109/TGRS.2017.2653186>
- Liu, C., Lay, T., Brodsky, E. E., Dascher-Cousineau, K., & Xiong, X. (2019). Coseismic rupture process of the large 2019 Ridgecrest earthquakes from joint inversion of geodetic and seismological observations. *Geophysical Research Letters*, 46(21), 11820–11829. <https://doi.org/10.1029/2019GL084949>
- Liu, J., Hu, J., Xu, W., Li, Z., Zhu, J., Ding, X., & Zhang, L. (2019). Complete three-dimensional coseismic deformation field of the 2016 central Tottori earthquake by Integrating left-and right-looking InSAR observations with the improved SM-VCE method. *Journal of Geophysical Research: Solid Earth*, 124(11), 12099–12115. <https://doi.org/10.1029/2018JB017159>
- Loveless, J. P., & Meade, B. J. (2011). Spatial correlation of interseismic coupling and coseismic rupture extent of the 2011 Mw= 9.0 Tohoku-oki earthquake. *Geophysical Research Letters*, 38(17), L17306. <https://doi.org/10.1029/2011GL048561>
- Magen, Y., Ziv, A., Inbal, A., Baer, G., & Hollingsworth, J. (2020). Fault rerupture during the July 2019 Ridgecrest earthquake pair from joint slip inversion of InSAR, optical imagery, and GPS. *Bulletin of the Seismological Society of America*, 110(4), 1627–1643. <https://doi.org/10.1785/0120200024>
- Michel, R., & Avouac, J. P. (2002). Deformation due to the 17 August 1999 Izmit, Turkey, earthquake measured from SPOT images. *Journal of Geophysical Research: Solid Earth*, 107(B4), ETG-2. <https://doi.org/10.1029/2000JB000102>
- Michel, R., Avouac, J. P., & Taboury, J. (1999). Measuring near field coseismic displacements from SAR images: Application to the Landers earthquake. *Geophysical Research Letters*, 26(19), 3017–3020. <https://doi.org/10.1029/1999GL900524>
- Milliner, C., & Donnellan, A. (2020). Using daily observations from Planet Labs satellite imagery to separate the surface deformation between the 4 July Mw 6.4 foreshock and 5 July Mw 7.1 mainshock during the 2019 Ridgecrest earthquake sequence. *Seismological Research Letters*, 91(4), 1986–1997. <https://doi.org/10.1785/0220190271>
- Okada, Y. (1992). Internal deformation due to shear and tensile faults in a half-space. *Bulletin of the Seismological Society of America*, 82(2), 1018–1040. <https://doi.org/10.1785/BSSA0820021018>
- Parsons, T., Ji, C., & Kirby, E. (2008). Stress changes from the 2008 Wenchuan earthquake and increased hazard in the Sichuan basin. *Nature*, 454(7203), 509–510. <https://doi.org/10.1038/nature07177>
- Petersen, M. D., Frankel, A. D., Harmsen, S. C., Mueller, C. S., Haller, K. M., Wheeler, R. L., et al. (2014). Documentation for the 2014 update of the United States national seismic hazard maps. *U.S. Geological Survey Open-File Report*. 2014-1091. <https://doi.org/10.3133/ofr20141091>
- Pinel-Puysségur, B., Grandin, R., Bollinger, L., & Baudry, C. (2014). Multifaulting in a tectonic syntaxis revealed by InSAR: The case of the Ziarat earthquake sequence (Pakistan). *Journal of Geophysical Research: Solid Earth*, 119(7), 5838–5854. <https://doi.org/10.1002/2013JB010564>
- Planet Team. (2017). *Planet application Program Interface: In space for Life on Earth*. Retrieved from <https://www.planet.com/markets/education-and-research/>
- Pollitz, F. F., Murray, J. R., Svarc, J. L., Wicks, C., Roeloffs, E., Minson, S. E., & Mencin, D. (2020). Kinematics of fault slip associated with the 4–6 July 2019 Ridgecrest, California, earthquake sequence. *Bulletin of the Seismological Society of America*, 110(4), 1688–1700. <https://doi.org/10.1785/0120200018>
- Ragon, T., Sladen, A., Bletery, Q., Vergnolle, M., Cavalié, O., Avallone, A., & Delouis, B. (2019). Joint inversion of coseismic and early post-seismic slip to optimize the information content in geodetic data: Application to the 2009 Mw 6.3 L'Aquila earthquake, Central Italy. *Journal of Geophysical Research: Solid Earth*, 124(10), 10522–10543. <https://doi.org/10.1029/2018JB017053>
- Ross, Z. E., Idini, B., Jia, Z., Stephenson, O. L., Zhong, M., Wang, X., & Jung, J. (2019). Hierarchical interlocked orthogonal faulting in the 2019 Ridgecrest earthquake sequence. *Science*, 366(6463), 346–351. <https://doi.org/10.1126/science.aaz0109>
- Simons, M., Fialko, Y., & Rivera, L. (2002). Coseismic deformation from the 1999 Mw 7.1 Hector Mine, California, earthquake as inferred from InSAR and GPS observations. *Bulletin of the Seismological Society of America*, 92(4), 1390–1402. <https://doi.org/10.1785/0120000933>
- Socquet, A., Hollingsworth, J., Pathier, E., & Bouchon, M. (2019). Evidence of supershear during the 2018 magnitude 7.5 Palu earthquake from space geodesy. *Nature Geoscience*, 12(3), 192–199. <https://doi.org/10.1038/s41561-018-0296-0>
- Sudhaus, H., & Sigurjón, J. (2009). Improved source modelling through combined use of InSAR and GPS under consideration of correlated data errors: Application to the June 2000 Kleifarvatn earthquake, Iceland. *Geophysical Journal International*, 176(2), 389–404. <https://doi.org/10.1111/j.1365-246X.2008.03989.x>
- Tizzani, P., Castaldo, R., Solaro, G., Pepe, S., Bonano, M., Casu, F., & Sansosti, E. (2013). New insights into the 2012 Emilia (Italy) seismic sequence through advanced numerical modeling of ground deformation InSAR measurements. *Geophysical Research Letters*, 40(10), 1971–1977. <https://doi.org/10.1002/grl.50290>
- Tung, S., Shirzaei, M., Ojha, C., Pepe, A., & Liu, Z. (2021). Structural Controls over the 2019 Ridgecrest earthquake sequence investigated by high-Fidelity elastic models of 3D velocity structures. *Journal of Geophysical Research: Solid Earth*, 126(7), e2020JB021124. <https://doi.org/10.1029/2020JB021124>
- U. S. Geological Survey. (2019a). *Earthquake catalog released by U. S. Geological Survey*. Retrieved from <https://earthquake.usgs.gov/earthquakes/eventpage/ci38443183/executive>
- U. S. Geological Survey. (2019b). *Earthquake catalog released by U. S. Geological Survey*. Retrieved from <https://earthquake.usgs.gov/earthquakes/eventpage/ci38457511/executive>
- Van Puymbroeck, N., Michel, R., Binet, R., Avouac, J. P., & Taboury, J. (2000). Measuring earthquakes from optical satellite images. *Applied Optics*, 39(20), 3486–3494. <https://doi.org/10.1364/AO.39.003486>
- Wang, K., & Bürgmann, R. (2020). Co- and early postseismic deformation due to the 2019 Ridgecrest earthquake sequence constrained by Sentinel-1 and COSMO-SkyMed SAR data. *Seismological Research Letters*, 91(4), 1998–2009. <https://doi.org/10.1785/0220190299>

- Wang, K., Dreger, D. S., Tinti, E., Bürgmann, R., & Taira, T. A. (2020). Rupture process of the 2019 Ridgecrest, California Mw 6.4 foreshock and Mw 7.1 earthquake constrained by seismic and geodetic data. *Bulletin of the Seismological Society of America*, *110*(4), 1603–1626. <https://doi.org/10.1785/0120200108>
- Werner, C., Wegmüller, U., Strozzi, T., & Wiesmann, A. (2000). Gamma SAR and interferometric processing software. In *Proceedings of the Ers-Envisat Symposium* (Vol. 1620, p. 1620).
- Wessel, P., Smith, W. H., Scharroo, R., Luis, J., & Wobbe, F. (2013). Generic mapping tools: Improved version released. *Eos, Transactions American Geophysical Union*, *94*(45), 409–410.
- Wright, T. J., Lu, Z., & Wicks, C. (2004). Constraining the slip distribution and fault geometry of the Mw 7.9, 3 November 2002, Denali fault earthquake with interferometric synthetic aperture radar and global positioning system data. *Bulletin of the Seismological Society of America*, *94*(6B), S175–S189. <https://doi.org/10.1785/0120040623>
- Xu, C., Liu, Y., Wen, Y., & Wang, R. (2010). Coseismic slip distribution of the 2008 Mw 7.9 Wenchuan earthquake from joint inversion of GPS and InSAR data. *Bulletin of the Seismological Society of America*, *100*(5B), 2736–2749. <https://doi.org/10.1785/0120090253>
- Xu, W., Feng, G., Meng, L., Zhang, A., Ampuero, J. P., Bürgmann, R., & Fang, L. (2018). Transpressional rupture cascade of the 2016 Mw 7.8 Kaikoura earthquake, New Zealand. *Journal of Geophysical Research: Solid Earth*, *123*(3), 2396–2409. <https://doi.org/10.1002/2017JB015168>
- Xu, X., Sandwell, D. T., & Smith-Konter, B. (2020). Coseismic displacements and surface fractures from Sentinel-1 InSAR: 2019 Ridgecrest earthquakes. *Seismological Research Letters*, *91*(4), 1979–1985. <https://doi.org/10.1785/0220190275>